Auxotonic to Isometric Contraction Transitioning in a Beating Heart Causes Myosin Step-Size to Down Shift

Thomas P. Burghardt[1,2,*], Xiaojing Sun[1], Yihua Wang[1], and Katalin Ajtai[1]

November 2016

Revised January 2017

Revised February 2017 Accepted 12 March 2017

[1] Department of Biochemistry and Molecular Biology, Mayo Clinic Rochester, Rochester, MN 55905

[2] Department of Physiology and Biomedical Engineering, Mayo Clinic Rochester, Rochester, MN 55905

[*] To whom correspondence should be addressed. Email: burghardt@mayo.edu

Short Title: Myosin Step-Size Down Shifting in Contraction

Abstract

Myosin motors in cardiac ventriculum convert ATP free energy to the work of moving blood volume under pressure. The actin bound motor cyclically rotates its lever-arm/light-chain complex linking motor generated torque to the myosin filament backbone and translating actin against resisting force. Previous research showed that the unloaded in vitro motor is described with high precision by single molecule mechanical characteristics including unitary step-sizes of approximately 3, 5, and 8 nm and their relative step-frequencies of approximately 13, 50, and 37%. The 3 and 8 nm unitary step-sizes are dependent on myosin essential light chain (ELC) N-terminus actin binding. Step-size and step-frequency quantitation specifies in vitro motor function including duty-ratio, power, and strain sensitivity metrics. In vivo, motors integrated into the muscle sarcomere form the more complex and hierarchically functioning muscle machine. The goal of the research reported here is to measure single myosin step-size and step-frequency in vivo to assess how tissue integration impacts motor function.

A photoactivatable GFP tags the ventriculum myosin lever-arm/light-chain complex in the beating heart of a live zebrafish embryo. Detected single GFP emission reports time-resolved myosin lever-arm orientation interpreted as step-size and step-frequency providing single myosin mechanical characteristics over the active cycle. Following step-frequency of cardiac ventriculum myosin transitioning from low to high force in relaxed to auxotonic to isometric contraction phases indicates that the imposition of resisting force during contraction causes the motor to down-shift to the 3 nm step-size accounting for >80% of all the steps in the near-isometric phase. At peak force, the ATP initiated actomyosin dissociation is the predominant strain inhibited transition in the native myosin contraction cycle. The proposed model for motor down-shifting and strain sensing involves ELC N-terminus actin binding.

Overall, the approach is a unique bottom-up single molecule mechanical characterization of a hierarchically functional native muscle myosin.

KEYWORDS

Transgenic zebrafish cardiac ventriculum

Single cardiac ventriculum myosin detection in vivo

Native cardiac myosin mechanical characteristics

Strain dependent cardiac myosin detachment from actin

In vivo zebrafish cardiac myosin step-size

In vivo zebrafish cardiac myosin step-frequency

Introduction

The myosin motor protein powers the beating heart with transduction of ATP to mechanical work. Rationalizing “bottom-up” single myosin mechanics with “top-down” whole animal muscle physiology is indispensable to solving myosin’s structure/function paradigm for creating an ensemble capable nanomotor and to providing the insight into muscle disease mechanisms demanded by translational science. A time-resolved in vivo imaging approach characterizes single myosin mechanics in contracting striated muscle of live zebrafish embryos. It provides the means for linking bottom-up myosin characteristics to top-down muscle physiology or phenotype in the zebrafish embryo model for human muscle.

The myosin transducer has a globular head (subfragment 1 or S1) and tail domain that forms myosin dimers and assembles into thick filaments. Thick filaments interdigitate with actin thin filaments in striated muscle and slide relatively during contraction [1]. S1 contains ATP and actin binding sites and a swinging lever-arm that cyclically applies tension to power filament sliding while myosin is strongly actin bound. The lever-arm converts torque generated in the motor into linear displacement (step-size) and undergoes strain due to the resisting force. Strain affects the lever-arm and the bound essential and regulatory light chains (ELC and RLC). RLC stabilizes the lever-arm [2] and disease implicated RLC mutants lower velocity, force, and strain sensitivity suggesting they alter lever-arm processing of stress [3]. The ELC N-terminus binds actin to modulate myosin functionality [4] and step-size in cardiac muscle [5].

In published work, we tagged human ventricular cardiac RLC (MYL2) at the C-terminus with green fluorescent protein (HCRLC-GFP) then exchanged the chimer into permeabilized skeletal [6] or cardiac papillary muscle fibers [7]. Extensively and specifically exchanged myosin in these fibers supports native isometric contraction implying the GFP tag does not affect muscle contraction. The photoactivatable variant, HCRLC-PAGFP, was individually activated in the exchanged papillary muscle fibers isolating single myosins *in situ*. Super-resolved orientation of single myosin lever-arms was measured from fibers in rigor, relaxation, and active isometric conditions. Single molecule orientation was also measured for the exchanged HCRLC-PAGFP modified by disease linked mutations to the HCRLC [3]. The exchanged mutant HCRLC lowered lever-arm stiffness and impaired lever-arm transduction/mechanical-coupling.

The zebrafish embryo is transparent to visible light allowing deep imaging using wide field fluorescence microscopy with highly inclined (HILO) illumination [8]. In the present work, new transgenic zebrafish were created by inserting the HCRLC-GFP or HCRLC-PAGFP gene into the zebrafish genome and using the cmlc2 promoter to drive gene expression in the heart [9]. Transgenic zebrafish embryos had visible GFP expression confined to the heart ventricle and arranged in the striated pattern characteristic to myosin in cardiac muscle fiber sarcomeres indicating specific myosin binding. Embryonic and adult transgenic zebrafish have normal heart phenotype and function. At 3-4 days post fertilization (dpf), embryos expressing HCRLC-PAGFP were imaged using HILO to detect single cardiac myosin lever-arms in the beating heart. The native embryonic heart runs with ~120 beats per min (bpm) at room temperature. We slowed heart rate to ~60 bpm using a reversible anesthetic treatment affecting nervous controlled cardiac pacing and imaged single cardiac myosins at 10 frames per second. Usually one heart cycle was quantitated in 10 sequential images. Each image acquired light for slightly less than 100 ms. This sampling rate captured and quantitated interesting mechanical features of the single functioning cardiac myosins while faster frame rates failed to provide an adequate signal to noise (S/N) ratio profile for quantitation. Control imaging experiments were also conducted on relaxed hearts temporarily stopped by a higher dose anesthetic treatment. The heart contraction cycle separated into late relaxed (diastole and full heart), auxotonic active (early systole where cardiac force exceeds load), and isometric active (late systole before ejection where cardiac force equals load) phases with distinct myosin mechanical characteristics. Comparison of single myosin mechanics in auxotonic and isometric contraction suggests a new paradigm for mechanical regulation of force/velocity.

Myosin mechanical functionality in vitro and at the single molecule level precisely characterizes the essential myosin structure/function paradigm but in the absence of the other motors and proteins in the muscle sarcomere. The native myosin is more complex with potential for hierarchical coordinated functionality because of its structured environment. The zebrafish embryo model system provides opportunity for single molecule mechanical characterization of a naturally integrated cardiac myosin. We measure in vivo cardiac myosin lever-arm rotation and interpret data as the step-size and step-frequency. These metrics uniquely specify native myosin functionality for an unprecedented view into how tissue integration shapes motor function.

Materials and methods

A. Zebrafish sample preparations

Ethics.

Zebrafish embryos were produced and used in this study with approval from the Mayo Clinic Rochester Institutional Animal Care and Use Committee (protocol A47113).

Zebrafish adult ventricular cardiac myosin extraction and preparation.

2-6 adult wild type (WT or Zmys) 11 month old dominant leopa zebrafish were obtained from the Mayo Clinic Zebrafish Core Facility. Fish were anesthetized for 3-5 minutes using tricaine methanesulfonate (MS-222, 168 mg/L) then euthanized. Hearts were dissected by using forceps and the ventricle placed into 1.5 ml eppendorf tubes containing 40 μL/(5 hearts) SDS sample buffer (0.125 M Tris-HCL pH 6.8, 10% glycerol, 2% SDS, 5% ² -mercaptoethanol, and 0.5 mg/ml bromophenol blue). The tubes were vortexed, pelleted in the centrifuge, and heated to 95 ^{o}C for 5 minutes. The pellet was homogenized by hand using a pellet pestle then incubated at room temperature for 30 min. The supernatant containing the extracted and denatured cardiac tissue proteins were heated again to 95 ^{o}C for 5 minutes and loaded to a gel or stored in the freezer at -20 ^{o}C.

Zebrafish embryo cardiac myosin extraction.

Dpf 6 embryos (~80) were anesthetized for 3-5 minutes using tricaine then euthanized. Embryos were transfer into E3 water (5 mM NaCl, 0.17 mM KCl, 0.33 mM $CaCl_2$, 0.33 mM $MgSO_4$, 10^{-5} % methylene blue) onto a 16-well glass slide. The hearts were dissected under the microscope using two insulin needles and excess buffer removed. We added 2-3 μL 3% SDS sample buffer (without bromophenol blue) to each well then transferred the tissue to a 1.5 ml Eppendorf tube on ice. The tissue sample was centrifuged at low speed, denatured at 95°C for 5

min, sonicated for 2 min, incubated at room temperature for 30 min and then centrifuged with 14000g for 10 min at 4°C. Supernatant containing solubilized protein was concentrated using ice cold 20% trichloro acetic acid (TCA) precipitation, vortexed and incubated for 30 minutes on ice, centrifuged for 30 minutes at top speed in a microcentrifuge at 4 °C then the supernatant was carefully removed to avoid disturbing the pellet. We added 0.5 ml cold acetone to the pellet to remove traces of TCA, vortexed briefly, centrifuged for 15 minutes at top speed in microcentrifuge at 4 °C, removed supernatant and dried the pellet with nitrogen gas. Dried pellet was resuspended in 2% SDS sample buffer with bromophenol blue, boiled, centrifuged at low speed to remove particulate matter, then loaded on the gel or stored at -20 °C.

Transgenic animals expressing HCRLC-GFP or HCRLC-PAGFP.

We coinjected transposase mRNA and plasmid containing a Tol2 construct with the zebrafish cmlc2 enhancer and the gene for HCRLC-GFP or HCRLC-PAGFP into the cytoplasm of one-cell-stage embryos. Cmlc2 enhancer drives HCRLC-(PA)GFP expression specifically in cardiac muscle [9]. At 3-4 dpf, we screened embryos for green fluorescence excited by 405 nm transmitted light using a 10X objective. Selected embryos exhibiting (PA)GFP expression were raised to produce F0 adults according to standard rearing protocols in the zebrafish core facility. After three months, the founder fish (F0) were screened by outcrossing with wild type. The F1 embryo offspring were used for experiments or grown to maturity for an F2 generation.

Transgenic zebrafish had visible (PA)GFP expression confined to the heart and in the striated pattern similar to that in skeletal muscle of transiently expressed HCRLC-(PA)GFP using the UNC-45b enhancer [10, 11]. Wild type fish were incrossed as control and F1 transgenic fish were outcrossed with wild type producing F2 embryos. F2 transgenic GFP(+) or GFP(–) (TgGFP(+) or TgGFP(–)) embryos having strong or weak (PA)GFP expression in the heart were selected at 3-4 dpf. Transgenic animals are indicated by TgGFP for either GFP or PAGFP chromophores. Single myosin imaging is always performed with the PAGFP containing isoform.

Embryos were usually treated with 0.5 mM 1-phenyl 2-thiourea (PTU) at 1 dpf to inhibit melanogenesis. Experiments were conducted at room temperature (20-22 ^{o}C).

Cardiac functionality in zebrafish embryos.

Zebrafish embryo cardiac function was estimated at 3 dpf using an ellipsoid of revolution to approximate ventricle shape with long (*a*) and short (*b*) axes measured from movies of the functioning hearts [12]. Cardiac performance was described by 4 parameters consisting of heart rate, ventricle shortening fraction (SF), ventricle end systolic (smallest) volume, and ventricle end diastolic (largest) volume. The shortening fraction measures the maximum change in *a* relative to the longest *a* over a contraction cycle. Measurements were conducted on WT and transgenic embryos with and without PTU treatment.

Quantitation of HCRLC-(PA)GFP tagged myosin in zebrafish embryos.

Native zebrafish cardiac ventricular regulatory light chain ZRLC and HCRLC-(PA)GFP protein expression levels were measured using SDS-PAGE of expressed and extracted proteins. Quantities of purified embryonic myosin were too low to detect quantitatively on a Sypro Ruby stained gel hence we combined Sypro Ruby staining and protein immunoblotting. Purified native adult zebrafish ventricular cardiac myosin and an *in vitro* expressed HCRLC standard were run on adjacent lanes on an SDS-PAGE gel that was stained with Sypro Ruby. Intensity for the ZRLC and HCRLC bands were compared to estimate ZRLC quantity. Protein bands from an identical gel were transferred to a membrane for Western blotting using a primary RLC antibody (1:1000 dilution, product number 10906-1-AP, Proteintech, Chicago, IL)[13]. Antibody staining of the known amounts of ZRLC and HCRLC validated and calibrated the standardized immunoblotting protocol for their detection.

Myosin extracted from WT, TgGFP(–), and TgGFP(+) embryos were run on adjacent lanes on an SDS-PAGE gel then the proteins were transferred to a membrane for Western blotting using the RLC antibody. Intensities of the HCRLC-(PA)GFP and ZRLC bands were

converted to HCRLC-(PA)GFP and ZRLC amounts and combined into the replaced fraction, $ZRLC_{rep}$, given by,

$$ZRLC_{rep} = \frac{[HCRLC - GFP]}{[HCRLC - GFP] + [ZRLC]} \quad (1)$$

where […] indicates mole protein and all bands came from the TgGFP(+) embryos. Independently, the amount of ZRLC removed was measured relative to a β-actin loading standard in WT and transgenic embryos and using the RLC and a β-actin antibody (1:2000 dilution, product number 4967, Cell Signaling Technology, Danvers, MA,)[14]. The ZRLC fraction lost due to transgenesis, $ZRLC_{rem}$, is given by,

$$ZRLC_{rem} = \frac{[ZRLC]_{WT} - [ZRLC]_{TgGFP(+)}}{[ZRLC]_{WT}} \quad (2)$$

Experiments were conducted at room temperature (20-22 ^{o}C).

Single cardiac myosin imaging in a beating heart.

At 3-4 dpf, TgGFP(+) embryos were imaged to detect single cardiac myosin dynamics in the ventriculum. A TgGFP(+) embryo was placed in a 200 μm deep microfluidic channel constructed from polydimethylsiloxane **(**PDMS) with the channel side up and immersed in 20 μL of 30% Danieau Buffer (D-buffer, 17.4 mM NaCl, 0.21 mM KCl, 0.12 mM $MgSO_4$, 0.18 mM $Ca(NO_3)_2$, 1.5 mM HEPES, pH 7.6). We introduced stepwise concentrations of tricaine, up to 2000 mg/L, to reduce heart rate from 108-125 bpm to 50-60 bpm at 20 ^{o}C to facilitate single myosin imaging. Heart rate returned to normal immediately after flushing out the drug with fresh buffer and the drug cleared naturally from the embryo at ≥10 minutes. Heart rate was monitored in a stereo microscope at high magnification. When heart rate stabilized the bathing solution volume was drawn down to <6 μL and the microfluidic was inverted then placed on top of a #0 glass coverslip forming a water tight seal with the glass for imaging exactly as described [10]. Embryos were imaged over time at a 10 Hz frame rate to collect single molecule emission images from photoactivated RLC-PAGFP. Imaging sessions were completed within 10 min.

Heart rate was measured visually in the microscope every 2-3 min and remained constant at 50-60 bpm over the course of the experiment. Blood circulation in capillaries in the fish tail was also monitored every 2-3 min in the microscope by visualizing blood cell movement. Blood cell flow did not qualitatively change over the course of the experiment.

We briefly stopped the heart by raising tricaine to 2200 mg/l in the microfluidic containing the embryo then imaged the constantly-relaxed cardiac myosin.

B. *In Vivo* single myosin orientation quantitation

S1/GFP coordination and coordinates.

The ribbon structure in **Fig 1** shows the myosin heavy chain (MHC) in blue and black, RLC and ELC binding the lever-arm in red and silver, and the GFP moiety in green. GFP is linked to the RLC C-terminus by the white linker. The S1 structure represents human β-cardiac myosin from homology modeling [15] of its sequence using the chicken skeletal myosin S1 crystal structure 2mys [16]. The arrow indicates direction of the black section of the lever-arm α-helix symmetry axis where RLC binds. The GFP chromophore in the middle of the β-barrel is indicated in red. The red arrow at the chromophore is the emission dipole orientation.

Fig 1. The coordination of the GFP moiety (green) and its emission dipole moment (red arrow) with myosin S1 consisting of a heavy chain (blue and black), ELC (silver), and RLC (red). The portion of the lever-arm in the heavy chain appearing in black is the α-helix segment associated with the lever-arm orientation and depicted by the black arrow. The insert shows the time-resolved coordinates for GFP chromophore emission dipole moment in red and lever-arm helix in blue corresponding to spherical polar angles (β',α') and (β,α) defined relative to a fiber fixed frame.

The insert has a blue arrow with embedded black α-helix representing the lever-arm with coordinates (β,α) defined relative to the unique fiber symmetry axis (z) and arbitrary x-axis defining the fiber frame. The red arrow with embedded chromophore moiety represents the GFP chromophore emission dipole related to the lab frame by (β',α') and referred to as probe coordinates.

The fiber frame xz plane in **Fig 1** lies in the microscope focal plane and in the lab frame as shown in **Fig 2**. Lab and fiber frames are related to each other by a rotation through χ about the y-axis (y-axis not shown). Images of the heart shown in Results relate to the lab frame like the test pattern in **Fig 2**.

Fig 2. The fiber frame xz plane in Fig 1 lies in the microscope focal plane and in the lab frame as shown. Lab and fiber frames are related to each other by a rotation through χ. Images of the heart shown subsequently relate to the lab frame like the image of the test pattern.

Orientation super-resolution measured from tagged zebrafish muscle.

Zebrafish embryos confined to the microfluidic chamber were imaged with fluorescence from the cardiac tissue as described above. Single molecule fluorescence measurements from the photoactivated HCRLC-PAGFP tagged myosin lever-arms were made on an inverted microscope using highly inclined thin illumination (HILO) excitation exactly as described [10].

In all fluorescence experiments, pump and observation exciting laser light polarization is p-polarized and propagating perpendicular to the long dimension of the embryo. In the heart tissue the fiber symmetry axis is not fixed but redefined for each single myosin. A sparse population of probes is photoactivated to achieve the most selective orientation distribution of photoactivated probes by using the lowest practical pump beam intensity. We identified single molecule events by their quantized intensity change due to photoactivation or photobleaching over time. Orientation super-resolution of unit vector μ_e[A], the *emission* dipole moment of the activated single molecule, is determined by pattern recognition exactly as described [10].

Raw GFP fluorescence intensity vs time from RLC-PAGFP tagged myosin *in vivo* from beating and relaxed zebrafish embryo heart ventriculum under HILO illumination is shown in **Figs A& B** in S1 File. Single myosins are identified by their quantized intensity change of ~1000 photons per 0.1 second above background due to photoactivation and subsequent photobleaching to background. Photon counts indicate intensity integrated over the EMCCD camera 11x11 pixel array containing the photoactivated chromophore image. Video files for these single myosin instances are in S1-S4 Movies.

S1/GFP coordination.

The S1/GFP coordination of the zebrafish skeletal muscle was determined as described [10] and is shown in **Fig 1**. For the present study and using the same method, we checked the new dipole orientation data for relaxed and contracting muscle (summarized subsequently in RESULTS) for consistency with the S1/GFP coordination in **Fig 1**. We found that the new data is consistent with the previous data in selecting the S1/GFP coordination in **Fig 1** over other docked models.

In vivo step-size.

Single molecule images provided super-resolved orientation of the photoactivated RLC-PAGFP emission dipole in zebrafish cardiac muscle. Dipole orientations were computed from

images that were continuously recorded for 20-40 sec. Object spatial drift, if present, was removed by large frame image alignment prior to analysis. The time-resolved coordinates have dipole or lever-arm helix spherical polar angles (β',α') or (β,α) defined relative to a fiber fixed frame shown in the insert to **Fig 1**. They are the trajectories for a single dipole or lever-arm helix.

The arc subtended by, Φ, the angle a single lever-arm helix rotates in sequential time-correlated images defines a sequence of chords on a circle of diameter *L* equal to the lever-arm length indicated in **Fig 3**. Chord length is step-size, *d*, given by,

$$d = 2L\,Sin(\tfrac{1}{2}\Phi) \qquad (3)$$

Step-sizes computed by eq. 3 from many single myosin trajectories are summarized as a histogram of incremental step-lengths vs the number of observed events. Step-lengths distribute differently for various muscle physiological states. Cardiac muscle contraction separates into auxotonic and isometric phases depending on position in the heart beat cycle with the auxotonic phase early in systole when fibers are shortening but overall muscle position is relatively steady. Towards the end of systole, fiber shortening slows as force reaches isometric level and the muscle image sharpens to its peak S/N ratio.

Fig 3. Myosin S1 consisting of a heavy chain, ELC (blue), and RLC (yellow) performing a powerstroke with a lever-arm rotation while strongly actin bound. The arc subtended by, Φ, the angle a single lever-arm helix rotates in sequential images defines a sequence of chords on a circle of diameter *L* equal to the lever-arm length indicated. Chord length is step-size, *d*, given by eq. 3. The ELC N-terminal extension, shown actin bound at the end of the powerstroke, plays a major role in the proposed mechanism for strain sensing in the myosin.

During contraction muscle has single myosins cycling through lever-arm orientations for actin-disassociated (relaxed) and actin-associated (force generating) conformations. The relaxation phase in diastole is not identified in the beating heart cycle because the muscle translates sufficiently to leave focus. The relaxed phase is observed separately in the heart when its beat cycle is briefly interrupted by additional tricaine. Relaxed phase muscle has single myosins maintaining a mostly actin-dissociated form with statically and dynamically averaged lever-arm orientation that is non-stationary in its time sequence over sampling intervals of 100 ms. Myosin develops force with its lever-arm swing starting in the high free-energy actin bound state of the myosin most closely associated with auxotonic phase. Peak force has myosin strongly actin-bound either with ADP or after ADP release (strained rigor) most closely associated with isometric phase. Both force generating phases also contain contributions from detached (relaxed) myosins and their active counterpart (isometric with auxotonic phase or auxotonic with isometric phase) due to asynchronous myosin cycling.

We model the step-size distribution in auxotonic and isometric phases of the heartbeat, v_{au} and v_{is}, with linear combination of distributions composed of relaxed, v_{re}, and alternatively v_{is} and Δv_{au} for the auxotonic case or v_{au} and Δv_{is} for the isometric case, where Δv_{au} and Δv_{is} are unknown force developing homogeneous auxotonic and isometric phases of the heartbeat, subject to constraints,

$$\begin{aligned} \Delta \mathbf{v}_{au} &= \mathbf{v}_{au} - \boldsymbol{c}_1 \mathbf{v}_{is} - \boldsymbol{c}_2 \mathbf{v}_{re} \\ \Delta \mathbf{v}_{is} &= \mathbf{v}_{is} - \boldsymbol{c}_3 \mathbf{v}_{au} - \boldsymbol{c}_4 \mathbf{v}_{re} \end{aligned} \qquad (4)$$

for unknown constants c_j, j = 1, 2, 3, and 4. The relaxed and active step-size histograms, v_{re}, v_{is}, and v_{au} are the basis vectors covering probability space spanned by tagged lever-arm orientations. They have Poisson distributed noise randomly sampled while Δv_{is} and Δv_{au} are independently minimized for each trial by selection of c_j subject to constraints Δv_{au} , Δv_{is}, and c_j all ≥ 0 using constrained linear programing in Mathematica. We estimate the mean and variance for Δv_{is} and Δv_{au} at each point in the histogram from the family of residuals produced in the trials.

Pathway networks.

Qdot assaying of porcine β-ventricular myosin (βmys) indicated three unitary steps-sizes of ~3, ~5, and ~8 nm with relative step frequencies of ~13, 50, and 37% [17]. Similar results were obtained using the assay for adult zebrafish skeletal myosin step-size and step-frequency [11]. We proposed that the major 5 nm step is the default step identical to the dominant step in skeletal myosin [18], that the 8 nm step is somewhat less likely and different from the 5 nm step by involving an extra interaction with actin via the unique N-terminus extension of ELC [4, 19-21], and that the minor 3 nm step is the unlikely conversion of the 5 nm step to the full cELC bound 8 nm step. The 3 nm step is isolated in time from the 5 nm step by slow ADP dissociation hence we sometimes observe it as a separate step [22]. We tested the N-terminus of ELC for its ability to regulate step-size and/or step-frequency using βmys and mouse cardiac myosin with the α heavy chain (αmys) including: a 17 residue N-terminal truncated ELC in porcine ventricular myosin made by papain digestion [23] and a 43 residue N-terminal truncated human ELC expressed in a transgenic mouse heart [24]. ELC N-terminus truncation caused significant redistribution in the step-frequencies among the unitary steps compared to control. An ensemble containing mainly myosin with ELC missing its N-terminus had significantly lower probability for making the 8 nm step but higher probability for the 5 nm step in both porcine βmys mouse αmys. ELC N-terminus truncation had little effect on the unitary myosin step-sizes [5].

The earlier in vitro work was described by a model where the 3 nm step happened only after a 5 nm step occurred. Three pathways producing 5, 8, or 5+3 nm steps describe this 3-pathway network. The present in vivo work implies that the 3 nm step can also occur independently from the 5 nm step because we observe a 3 nm step-frequency that sometimes exceeds that for 5 nm step. Four pathways producing 5, 8, 5+3, and 3 nm steps describe the new 4-pathway network that is the basis for the new model discussed in RESULTS. The 4-pathway network is a superset of the 3-pathway network.

Relaxed myosin lever-arm orientation dynamics.

Relaxed myosin dimers in the cardiac thick filament form intra- and inter-dimer interactions thought to impact the in vivo muscle. Isolated myosin dimers exhibit the intra-dimer blocked and free head motif [25] within the hierarchical quasihelical thick filament structure [26]. The latter grants inter-dimer interactions stabilizing a globally regular but locally variable myosin 3D structure. Static variability is probably accompanied by dynamic dispersion as myosin monomers sample conformation space. We hypothesize that single myosin head dynamics observed in the relaxed zebrafish cardiac muscle results from the conformation space sampling. We estimate potential effects of conformation space sampling by using the tarantula myosin filament reconstruction (3jbh.pdb) as a model for relaxed cardiac muscle [27]. Single myosin measurements track lever-arm orientation relative to the thick filament axis using a specific region of the lever-arm helix equivalent to the black section of the human cardiac myosin lever arm in **Fig 1** (residues 808-827, tarantula sequence) that we estimate for the tarantula myosin. Thick filament axis orientation is estimated using a specific region of S2 (residues 943-962, tarantula sequence). Thick filament axis orientation computed from each of the 4 myosins in the tarantula structure estimates a probability density for variability in thick filament structure that we assume single myosins sample during the course of the time-resolved lever-arm orientation measurement. We estimate the relaxed lever-arm step-size by computing Φ for lever-arm orientation relative to random variates of the thick filament structure substituting for a time-dependent trajectory. Φ's are converted to step-size using eq. 3 and giving a step-size histogram comparable to observation.

Results

HCRLC-GFP stoichiometry in the zebrafish heart.

We detected the ZRLC and HCRLC-GFP protein content in WT and TgGFP(+) embryo and adult zebrafish hearts using SDS-PAGE and combining Sypro Ruby staining and immunoblotting for detection of protein content. **Fig 4** shows the Sypro Ruby stained and immunoblotted SDS-PAGE gels. The Sypro Ruby gel band intensities establish ZRLC content in a zebrafish adult heart extract relative to a known amount of in vitro expressed HCRLC (**panel a**). These samples produce calibrated blot intensities for HCRLC and ZRLC under a standardized protein immunoblotting protocol using the RLC antibody as described in Methods and previously [11]. The standards are compared to immunoblots from HCRLC-GFP and ZRLC in WT and TgGFP(+) embryos (**panel b**) to measure relative fractions of HCRLC-GFP and ZRLC content ($ZRLC_{rep}$, eq. 1). The relative amount of ZRLC in WT and TgGFP(+) embryo hearts confirmed ZRLC content removed ($ZRLC_{rem}$, eq. 2) by their comparison to control β-actin expression (**panel c**) as described in Methods and previously [11]. Results agree that $ZRLC_{rep} = 0.63 \pm 0.04$ where error is standard deviation for n=6. Each sample size has ~80 embryos.

Fig 4. **The Sypro Ruby stained and immunoblotted SDS-PAGE gels. The Sypro Ruby gel band intensities establish ZRLC content in a zebrafish adult heart extract relative to a known amount of in vitro expressed HCRLC (panel a).** These samples produce calibrated blot intensities for HCRLC and ZRLC under a standardized protein immunoblotting protocol using the RLC antibody as described in Methods and previously [11]. The standards are compared to immunoblots from HCRLC-GFP and ZRLC in WT and TgGFP(+) embryos (**panel b**) to measure relative fractions of HCRLC-GFP and ZRLC content ($ZRLC_{rep}$, eq. 1). The relative amount of ZRLC in WT and TgGFP(+) embryo hearts confirmed ZRLC content removed ($ZRLC_{rem}$, eq. 2) by their comparison to control β-actin expression (**panel c**).

Effect of HCRLC-GFP on zebrafish embryo heart contractility.

Fig 5 compares heart rate in beats per minute (BPM), shortening fraction (SF), and cyclical ventricle volume changes for WT and TgGFP(+) embryos in the presence (blue) and absence (black) of PTU. Error bars show standard deviation for *n* embryos. HCRLC-GFP incorporation into ~60% of the cardiac myosins in the heart has no significant impact on performance measured with these metrics. The PTU treatment inhibits melanogenesis and improves contrast in embryo heart images. It likewise has no significant impact on these metrics.

Fig 5. **Comparison of heart rate in beats per minute (BPM), shortening fraction (SF), and cyclical ventricle volume changes for WT and TgGFP(+) embryos in the presence (blue) and absence (black) of PTU treatment.** Error bars show standard deviation for *n* embryos.

Quantitation of embryonic zebrafish cardiac myosin lever-arm swing during the heart beat cycle.

At 3-4 dpf, TgGFP(+) embryos were imaged to detect single cardiac myosin dynamics in the ventriculum as described in METHODS. **Fig 6** shows a single frame from a movie and the averaged image of the beating heart where single molecule candidates are visible. This movie records ~6 sequential in-focus images of the sarcomeres followed by ~4 blurred images of shortening or otherwise moving sarcomeres and muscle fibers. In-focus

images show approximately isovolumetric contraction since muscle shortening follows. We observed that the S/N ratio of the single myosin fluorescence is largest at highest isometric force just before ejection. We use this feature to synchronize the cardiac cycle with fluorescence intensity. The 1-2 highest S/N images were used for quantitation of the near-isometric contraction phase. The remaining 4-5 in-focus images were used for quantitation of the auxotonic contraction phase. We also stopped the heart by raising tricaine to 2200 mg/l in the microfluidic containing the embryo then briefly imaged the constantly-relaxed cardiac myosin.

Fig 6. A single frame (left) and an averaged image of the heart (right) running at 50-60 bpm.

Single myosin candidate images are isolated into 11x11 pixel movies from which the total intensity of each frame is plotted over time. From the intensity vs time plots we identify the single molecule photoactivation and photobleaching events thus qualifying the single myosin movie for inclusion into the data set. **Figs A& B** in S1 File indicate intensity vs time plots for single myosins in active and relaxed cardiac muscle.

The single molecule intensity patterns from zebrafish embryo single cardiac myosins were fitted using the pattern recognition algorithm and subjected to orientation super-resolution analysis [28, 29]. Time-resolved coordinates, having dipole or lever-arm helix spherical polar angles (β',α') or (β,α) defined relative to a fiber fixed frame (**Fig 1**), indicate the trajectories for a single dipole or lever-arm. Dipole orientation data impacts the best choice for the S1/GFP coordination. The new data representing cardiac myosin in relaxed and active muscle is consistent with the previous data selecting the S1/GFP coordination in **Fig 1** over other docked

models [10, 11]. The arc subtended by, Φ, the angle a single lever-arm helix rotates in sequential images defines a sequence of chords on a circle of diameter *L* equal to the lever-arm length indicated in **Fig 3**. Chord length is step-size, *d*, given by eq. 3.

We modeled the force developing homogeneous auxotonic and isometric phases, Δv_{au} and Δv_{is} using eq. 4 and as described there. Known relaxed and active step-size histograms v_{re}, v_{au}, and v_{is} are assigned their Poisson distributed noise and randomly sampled while $\triangle v_{au}$ or Δv_{is} are minimized for each trial by selection of c_1 and c_2 or c_3 and c_4 subject to constraints c_1, c_2, c_3, c_4, $\triangle v_{au}$, and Δv_{is} all ≥ 0 using constrained linear programing. We estimate average and variance for $\triangle v_{au}$ and Δv_{is} from the trials. Standard deviation of the mean for $\triangle v_{au}$ or Δv_{is} is computed for 15 or 24 cardiac muscle fibers from 8 or 6 embryos and corresponding to 1251 or 1436 single myosin coordinates from relaxed and active hearts, respectively.

Fig 7 panels a-c display the cardiac myosin cycle from homogeneous auxotonic ($\triangle v_{au}$), through homogeneous near-isometric ($\triangle v_{is}$), to relaxation (v_{re}). **Fig 7 panel d** compares in vivo skeletal myosin step-size in relaxation from zebrafish embryo trunk muscle [11] with the cardiac data. The skeletal (red) contrasts with the cardiac relaxed muscle (black) from the present study (**panels c or d**) where the relaxed cardiac myosins occupy a 2x larger step-size domain. The difference could be due to the higher time-resolution in the cardiac measurement or to other factors distinguishing cardiac and skeletal myosin. The former could convert a stationary relaxed lever-arm orientation observed from the in vivo skeletal myosin time-resolved trajectory into the non-stationary one observed for the in vivo cardiac myosin provided dynamic/static myosin rotational relaxation time was poised between 100 and 1000 ms. This is unlikely because rotation relaxation of the myosin head in relaxed skeletal muscle is on the order of 300-1000 ns [30]. Considering the latter, inter- and intra-myosin dimer interactions are known to impact relaxed myosin structure in cardiac thick filament [26] possibly leading to the more widely statically and dynamically distributed relaxed lever-arm [27]. We simulated the potential effect of thick filament interactions on relaxed cardiac myosin apparent step-size using the tarantula skeletal muscle thick filament structure as a model [27] and the approach described in METHODS. **Fig 7 panel d** compares simulated (blue) and observed relaxed myosin step-size distributions from cardiac (black and same as in **panel c**) and skeletal (red) zebrafish embryo muscle. Agreement between the cardiac muscle and simulated curves implies that inter- and intra-myosin dimer

interactions impacting relaxed myosin structure in cardiac thick filament could explain the larger apparent step-size domain compared to the zebrafish skeletal muscle. While thick filament dispersion is likely also manifest in the skeletal muscle, our data suggests cardiac muscle myosin is dynamically distributed more widely on the 100 ms time scale.

Fig 7. **Panels a-c. In vivo cardiac myosin active cycle from auxotonic (force developing), through near-isometric (maximum force), to detachment (relaxation) phases.** Error bars indicate standard deviation of the mean for 15 or 24 cardiac muscle fibers from 8 or 6 embryos and corresponding to 1251 or 1436 single photoactivated myosin coordinates from relaxed and active hearts, respectively. Dotted vertical lines in panels **a & b** define the boundaries between step-size frequencies computed from areas under the curves for nominal steps of 0, 3, 5, and 8 nm (nominal step-size corresponds to the in vivo measured step-sizes of 0, 2, 4, and 6 nm as indicated on the x-axis legend). Areas at step-size boundaries are split equally between adjoining step-sizes. **Panel d**. Simulated (blue) and observed (black and same as in **panel c**) relaxed cardiac (ca) myosin step-size distribution. Simulation is based on dispersion of thick filament structure surmised from the atomic model of Alamo et al. [27] as described in METHODS. In vivo relaxed skeletal (sk) myosin step-size from zebrafish embryo trunk muscle (red) is shown for comparison **[31]**.

Time-resolved single molecule experiments follow myosin through its cycle in real time. These data are summarized with event/step-size histograms also indicating step-frequency for the three unitary step-sizes observed. In vivo step-size from homogeneous auxotonic and near-isometric cardiac myosin in **Fig 7 panels a & b** indicates step-size probabilities peaking at ~2, 4

and 6 nm paralleling the unloaded in vitro estimates of ~3, 5, and 8 for zebrafish skeletal myosin [11]. Strain in the active cardiac myosin under load probably affects the apparent in vivo step-sizes by compacting the lever-arm rotation angle Φ. **Fig 7 panel b** indicates a force bearing 0 length step-size in the near-isometric phase that is unique to the in vivo myosin.

Contraction cycle 4-pathway model.

Fig 8 indicates a 4-pathway network producing 3, 5, and 8 nm steps (2, 4, and 6 nm in vivo) over the in vivo myosin cycle. Actin weakly attached states fall outside the dashed green box. Quantities f_i are myosin flux through the cycle with green and black indicating observed and computed values. We have shown previously using the Qdot assay that the basis of the 3, 5 and 8 nm unitary steps is the actin binding of the ELC N-terminus in a mechanism summarized in the figure [5]. Ignoring for a moment the shaded regions containing hypothetical strain dependent states, the bottom pathway with flux f_4 performs the 5 nm step with release of product (Pi followed by ADP) but without attachment of the ELC N-terminus then ATP binding and actin detachment (f_5). Alternatively, following a 5 nm step, slow ADP dissociation allows the ELC N-terminus to occasionally bind actin to make a subsequent 3 nm step with ADP release (f_7) then ATP binding and actin detachment. The top pathway (f_1) performs the 8 nm step with product release (Pi followed by ADP) and attachment of the ELC N-terminus then ATP binding and actin detachment. Pathways just described were identified previously in the context of the Qdot assay [5]. The middle pathway has flux f_3 and a 3 nm step not preceded by a 5 nm step. It has Pi release without strong actin binding to avoid a 5 nm step, followed by ADP bound myosin strong actin attachment, then the 3 nm displacement. It is populated when actin has sufficient resisting force explaining its absence from the unloaded Qdot assay experiments. It is needed to accommodate the real situation when the quantity of 3 nm steps exceeds that of 5 nm steps. For each myosin state, blue vector **v** at the end of the myosin lever-arm is positive net force on, and positive velocity of, the thick filament in units where amplitudes are equal.

Fig 8. **Myosin flux through the 4-pathway network contrasting 3 phases of muscle contraction in the beating heart.** Myosin begins and ends detached from actin and with ATP bound in the contraction cycle. The green box with dashed line boundaries group the strong actomyosin bound states. Blue vector **v** at the end of the myosin lever-arm is positive net force on, and positive velocity of, the thick filament in units where amplitudes are equal. Fluxes through the network, f_i, differ depending on contraction phases (values in **Table 1**). Measured values for f_i are in green while computed values are indicated in black. Four pathways cross from beginning to end of the contraction cycle. The top pathway populated by flux f_1 executes an 8 nm step-size. The middle pathway populated by flux f_3 executes a 3 nm step-size. It releases Pi while weakly actin bound without doing work. The bottom pathway populated by flux f_4 is branched and executes 5 or 5+3 nm step-sizes. The branch from the bottom pathway is populated by flux f_7 and executes the 5+3 nm step-size. Strain sensitivity is modeled with mechanisms in two subpathways within the shaded regions. The upper mechanism is populated by fluxes f_2 and f_8 from the 8 and 3 nm steps when the ELC N-terminus binds actin for actomyosin in rigor. The taut (blue line), intermediate (green curve), and slack (red wave) ELC N-terminus for muscle in near-isometric, auxotonic, or unloaded phases have high, modest, or zero strain when net force **v** is zero in isometric, intermediate in auxotonic, or high in unloaded phase. The linear (blue) actin bound ELC N-terminus is proposed to inhibit ATP binding by lowering active site accessibility for ATP at the small arrow near the myosin head. Inhibited ATP binding extends actomyosin attachment time indicated by the clock icon and quantitated in our single myosin measurements as a 0 length step. The lower mechanism is populated by flux f_6 from the 5 nm step with ADP bound. Near-isometric, auxotonic, or unloaded phases have high, intermediate, or zero strain (of an unspecified myosin element) when net force is zero, intermediate, or high. Strain lowers ADP release rate. Short duration ADP rate inhibition flux, f_7, leaves to continue with the 3 nm step. Long duration ADP rate inhibition flux, $f_6 - f_7$, continues with the 0 length step. For either the ATP accessibility or ADP release rate mediated mechanisms (top or bottom strain sensing mechanisms), low net force inhibits myosin cycling by extending the time myosin is strongly actin bound by $>2\Delta t$.

Shaded regions in **Fig 8** contain models for long lived strained conformation states in two mechanisms. The upper mechanism is populated by fluxes f_2 and f_8 from the 8 and 3 nm steps when the ELC N-terminus binds actin and the myosin is in rigor. The taut (blue) versus slack (red) ELC N-terminus in near-isometric versus unloaded phases have high versus zero strain when net force (or velocity) is zero in isometric contraction versus >> 0 in unloaded conditions. Taut ELC N-terminus is proposed to strain myosin in rigor (strained rigor) inhibiting ATP binding by lowering active site ATP accessibility as indicated by the size of the opening at the arrow near the myosin head. Delayed ATP binding and detachment (for >2Δt) gives a state observed as the force bearing 0 length step (f_2 or f_8). Slack ELC N-terminus has only prompt ATP binding and actin detachment ($f_2 = f_8 = 0$). The lower mechanism is populated by flux f_6 from ADP bound myosins. Near-isometric versus unloaded phases have high versus zero strain when net force (or velocity) is zero in isometric contraction versus >> 0 in unloaded conditions. ADP release rate is diminished in the former case. Spontaneously slow ADP release that is not caused by strain allows additional time (~Δt) for the ELC N-terminus to bind actin and perform a 3 nm step. Flux f_7 follows this pathway. The remainder has delayed ADP release caused by strain (for >Δt) giving a state observed as a 0 length step. Unloaded conditions without strain have $f_6 = 0$ with prompt ATP binding and actin detachment (f_5) or a subsequent 3 nm step (f_7). For either mechanism, the net effect of high strain is to inhibit myosin cycling by extending the time by >2Δt that myosin is strongly actin bound giving the 0 length step state with a summed flux, $f_9 = f_2 + f_6 - f_7 + f_8$, measured by the data in **Fig 7**.

The force bearing 0 length step-size involves a temporary diversion of myosin flux into an inhibited state that does not provide a parallel pathway though the myosin active cycle. Traditional normalization has step-frequencies for the 3, 5, and 8 nm steps summing to 1 such that,

$$x_0 = \frac{\omega_0}{1-\omega_0}, \quad x_3 = \frac{1-(\omega_0+\omega_5+\omega_8)}{1-\omega_0}, \quad x_5 = \frac{\omega_5}{1-\omega_0}, \; and \; x_8 = \frac{\omega_8}{1-\omega_0} \quad (5)$$

where ω_0, ω_3, ω_5, and ω_8 are areas under the probability curves for the ~0, 3, 5, and 8 nm step-sizes indicated in **Fig 7 panels a & b**. Flux values for all phases studied are summarized in **Table 1**. The caption provides additional details about quantitation of ω_0, ω_3, ω_5, and ω_8 from **Fig 7** and the optimization routine to obtain fluxes not directly observed.

Table 1 [a]. **Cardiac myosin flux through *in vivo* active cycle in 3 phases.**

	Step-probability			
phase	ω_0	ω_3	ω_5	ω_8
Unloaded (n=27)	0	0.13±0.04	0.50±0.09	0.37±0.08
Auxotonic (24)	0.03±0.12	0.44±0.27	0.45±0.17	0.08±0.04
Near-isometric (24)	0.33±0.02	0.54±0.04	0.12±0.03	0.01±0.01

	Flux									
phase	f_1	f_2	f_3	f_4	f_5	f_6	f_7	f_8	f_9	f_{10}
Unloaded	39±7	0	5±8	56±9	43±11	13±9	13±9	0	0	18±12
Auxotonic	10±5	2±1	31±23	59±23	37±21	29±11	21±9	3±4	13±11	52±22
Near-isometric	2±1	1±1	80±5	18±5	12±3	15±4	6±2	42±5	52±4	86±3
notes	input & output	$\leq f_1$	input	input	output f_4-f_7	$\leq f_5$	5→3 f_4-f_5	$\leq f_{10}$	$f_2+f_6+f_8$	output f_3+f_7

[a] **Table 1** (top) has step-probabilities measured from the data in **Fig 7 panels a & b** for 0, 3, 5,

and 8 nm steps (0, 2, 4, and 6 nm in vivo) computed from areas under the probability curves and for auxotonic and isometric phases. Areas are defined in the figure panels by the vertical dotted lines with probability at the step-size boundaries split equally between adjoining areas. Data for the unloaded phase is taken from earlier in vitro work on porcine ventricular myosin (MYH7) [5, 17]. Step-probabilities $\{\omega_0, \omega_3, \omega_5, \omega_8\}$ are normalized to sum to 1. Errors are standard deviation for (n) replicates. **Table 1** (bottom) has flux quantities, f_i, for the 4 step-size network defined in the **Fig 8** model. Several flux values relate to known step-frequencies using eq. 5 and where $f_1 = x_8$, $f_4 = x_5$, $f_9 = x_0$, and $f_{10} = x_3$. Other fluxes are surmised by using constraints. Flux conservation equality constraints include (total input) $f_1+f_3+f_4 = f_1+f_5+f_{10}$ (total output), $f_4 = f_5+f_7$ (5 nm step input detaches or continues to 3 nm step), $f_3+f_7 = f_{10}$ (3 nm step input sums with 5/3 nm step conversion then detaches with a 3 nm step), and $f_2+f_6 -f_7+f_8 = f_9$ (total 0 length steps). The problem is under determined by equality constraints hence it is solved in two steps: first using equality constraints eliminating 4 parameters, second using 3 equality constraints relating f_2, f_3, f_5, f_6, f_7, and f_8 and inequality constraints for these variables. Inequality constraints are $f_2 \le x_8$, $f_2 \le x_0$, $f_3 \ge x_3-x_5$, $f_3 \le x_3$, $f_5 \le x_5$, $f_6 \le x_5$, $f_7 \le f_6$, $f_7 \le x_5$, $f_8 \le x_3$, $f_8 \le x_0$, and all unknowns ≥ 0. The latter equality and inequality constraints are sufficiently restrictive to identify convergent solutions for the fluxes for each phase using constrained linear programing in Mathematica. We estimate standard deviations for fluxes within all constraints by generating random variates using normal distributions for $\{\omega_0, \omega_3, \omega_5, \omega_8\}$, computing x_0, x_3, x_5, and x_8 using eq. 5, then solving for the unknown flux values. Flux errors are standard deviation for (n) replicates. Total input (or equivalently total output) is re-normalized to 100% post hoc facilitating comparison between phases.

Step-frequencies quantitate step-size probability but they are ambiguous in the 4-pathway network since a particular myosin passing through its cycle could do 5 then 3, 5, or 3 nm steps. The relative fluxes through the 4 pathways in **Fig 8** are unique in this regard. **Table 2** summarizes myosin 4-pathway flux for the beating zebrafish embryo heart. They accommodate

the new step-size generating model in which the 3 nm step has a dedicated input pathway in addition to the 3 nm step dependent on input to the 5 nm step.

Table 2. **Myosin flux through the 4-pathway network in a zebrafish embryo beating heart.**

	step-size (in nm) [a] and normalized flux [b]			
phase	8 nm	5 nm (only)	3 nm (only)	5 then 3 nm
Unloaded (n=27) [c]	39±7	43±11	5±21	13±9
Auxotonic (24)	11±5	43±22	25±31	21±9
Near-isometric (24)	2±1	12±3	80±6	6±2

[a] Step-sizes in vivo are ~6, 4, and 2 nm.

[b] Fluxes reflect total input or output at 100% for each phase. Errors are standard deviation for (n) replicates.

[c] Data for the unloaded phase is taken from earlier in vitro work on porcine ventricular myosin (MYH7) [5, 17].

The unloaded phase in **Fig 8** occupies the earliest part of the force producing cycle when velocity and net force are positive and largest. We model it with characteristics from the unloaded in vitro assay and under the assumption that there are no 0 length steps ($f_9 = 0$). The ELC N-terminus is shown as a slack curve (red) indicating it does not undergo enhanced or prolonged strain for large velocity and net force (**v** >> 0). Input flux separates 39/5/56 into the 8, 3, and 5 nm step pathways (f_1, f_3, and f_4) where f_1 and f_4 are derived initially from the traditional step-frequency percentages (ω_8 and ω_5) of 37 and 50% then undergo input normalization to

accommodate unknown f_3. A fraction of myosins completing the 5 nm step release ADP with the attachment of the ELC N-terminus ($f_6 = f_7$) to perform a subsequent 3 nm step. These are joined by the direct contribution (f_3) together giving 18% of the output flux f_{10}. The pure 5 nm step output (f_5) contributes 43% and the 8 nm step (f_1) independently contributes 39% of the output flux. Output flux is $f_1+f_5+f_{10} = 100\%$.

The auxotonic phase in **Fig 8** produces lower velocity and net force than the unloaded phase. It is characterized directly from the in vivo step-size data (**Fig 7**). The total 0 length step flux (f_9) is approximately equivalent to error (**Table 1**). The observation that few 0 length steps occur in the auxotonic phase lends credibility to the assumption that the unloaded phase makes no 0 length steps. The ELC N-terminus is shown as a nearly taut curve (green) representing modestly enhanced or prolonged strain when velocity and net force are modestly positive ($\mathbf{v} > 0$). Input flux separates 10/31/59 into the 8, 3, and 5 nm step pathways (f_1, f_3, and f_4). The input flux of the 5 nm step (f_4) is about equal to that in the unloaded phase but more of these myosins also undergo the coupled 3 nm step (f_7). These are joined by the direct contribution (f_3) together giving all of the output flux f_{10}. Thus the 3 nm step-size flux enjoys a ~3-fold increase over the unloaded phase. The 8 nm step suffers a 4-fold reduction in flux from 39 to 10% (f_1) when compared to the unloaded phase. The modest net force probably lowers ADP release rate sufficiently to shift myosin flux into f_7 favoring the 3 nm step pathway over the terminal 5 nm step pathway (f_5) but insufficiently to produce significant 0 length steps.

The near-isometric phase in **Fig 8** produces near zero velocity and net force. It is also characterized directly from the in vivo step-size data (**Fig 7**). The 0 length step flux at 52% (f_9) indicates that half of the cardiac myosins have inhibited detachment from actin due to strain. The ELC N-terminus is shown as a taut curve (blue) representing strongly enhanced or prolonged strain when velocity and net force are nearly zero ($\mathbf{v} \approx 0$). Input flux separates 2/80/18 into the 8, 3, and 5 nm step pathways (f_1, f_3, and f_4). The terminal 5 nm step-size flux (f_5) is low with 3 out of 4 myosins first undergoing strain dependent inhibition. The 3 nm step-size flux (f_{10}) accounts for most myosins at 86%, a large increase over auxotonic phase, but in this case most myosins (80%) arrive there by the direct route with f_3. The 8 nm step-size flux at 2% (f_1) is negligible. The zero net force is proposed to enhance or prolong ELC N-terminus strain in strained rigor to inhibit ATP binding and strongly shift myosin flux (f_6 and f_8) to favor the 0 length step

pathways. High flux through the 3 nm step-size pathway implies it clears the backlog of high free energy or tension producing myosins at near-isometric force as it can continue to move myosins through the active cycle when the other step-size pathways cannot indicating how the motor down shifts to smaller step-size pathways in the near-isometric phase.

Dominance of the 3 nm step in isometric contraction implies a deeper significance because this step results from actin binding of the ELC N-terminus. It implies the ELC N-terminus is the nanomotor ratchet that locks the myosin into a force bearing state (0 length step) until there is additional forward movement from another motor in the ensemble or when loading force decreases with the movement of blood such that the ratchet can release locked myosin to complete its ATPase cycle.

Discussion

Myosin in striated muscle transduces ATP free energy into the mechanical work of moving actin. It does so using cyclical rotary movement of the lever-arm/light-chain complex linking motor generated torque to the myosin filament backbone. The linear actin displacement due to lever-arm rotation defines the unitary myosin step-size. The essential in vitro myosin structure/function paradigm is captured by its single molecule mechanical characteristics measured using the Qdot assay characterizing motor step-size and step-frequency [32]. Muscle myosin performance beyond the essential structure/function paradigm is influenced by self-assembly and integration with other motors and proteins in the muscle sarcomere. The native integrated myosin, with potential for hierarchical coordinated functionality and regulation because of its structured environment, was investigated here with cardiac myosin in live zebrafish. We developed tools to measure and interpret in vivo single cardiac myosin lever-arm rotation in a beating heart and estimate the cardiac myosin step-size and step-frequency. These metrics provide unprecedented insight into native cardiac myosin structure/function.

Myosin unitary step-size and rotation (tilt) has been studied for a long time. Ensemble myosin techniques used active muscle quick release or quick stretch length transients followed by time-resolved measurements of force [33], myosin polarized fluorescence [34-36], and X-ray diffraction [37] to compute the average unitary step-size or tilt under various loads. Later, because of the laser trap [38], in vitro single myosin step-size measurements became a standard and loaded myosin had a single, shorter, step-size [39]. Interest remained in ensemble force and X-ray methods because they worked on live excised tissue where average step-size was likewise shown to shorten with load. With transgenic zebrafish and the activatable tag on myosin, measuring in vivo single myosin step-size is now possible as we report here. Although our work on in vivo cardiac myosin extends our in vitro work where we identified the 3 unitary step-sizes and their step-frequencies [17], there is also overlap and general agreement with the ensemble average step-size measurements indicating a shorter average step with higher load. Comparing ensemble average and single myosin results we find there are three critical distinctions. We report that the average step-size shortens under increasing load due to shifting frequencies among short, intermediate, and long unitary step-sizes, we directly observe the force bearing 0 length step, and the mechanism for how all of it is accomplished involving ELC N-terminus actin

747 binding follows directly from earlier in vitro single myosin measurements [5, 17]. The latter
748 indicates that shifting step-frequencies to favor the short step is a downshifting maneuver caused
749 by the ratcheting effect of the actin bound ELC N-terminus also showing that the in vitro and in
750 vivo systems closely correlate.

751 **Fig 7 panel d** contrast in vivo relaxed cardiac and skeletal myosin apparent step-size
752 probabilities indicating a more orientationally dynamically dispersed native cardiac myosin
753 lever-arm. Cardiac myosin is known to maintain various special conformations in relaxation
754 related to a super-relaxation state [26, 40-42] and the effect of RLC phosphorylation [43]. These
755 circumstances could impact relaxed myosin conformational sampling. We modeled this effect
756 using the structural heterogeneity indicated in an atomic model reconstruction for tarantula
757 myosin filament [27] and estimated relaxed lever-arm apparent step-size by computing Φ for
758 random variates of the thick filament structure substituting for a time-dependent trajectory. Φ's
759 are converted to step-size using eq. 3 giving a pseudotime-dependent single myosin signal that
760 compares favorably to observation as indicated in **Fig 7 panel d**. While divergence of in vivo
761 lever-arm time-dependent trajectories in cardiac and skeletal muscle could be from the higher
762 time-resolution in the new cardiac measurement, earlier work with relaxed porcine cardiac
763 ventricular myosin lever-arm orientation from permeabilized papillary muscle fibers indicated a
764 similar pattern when compared to skeletal muscle at equivalent time resolutions [10]. We
765 conclude that the divergence of in vivo cardiac and skeletal observations on relaxed muscle
766 relates to the special conformations of cardiac thick filament.

767 Myosin translates actin when the two proteins are strongly bound. In the Qdot assay,
768 unitary actomyosin interactions are characterized in vitro with super-resolution microscopy [17].
769 Qdot assaying of porcine β-ventricular myosin (βmys) indicated three unitary steps-sizes of ~3,
770 5, and 8 nm with relative step frequencies of ~13, 50, and 37% [17]. Similar results were
771 obtained using the assay for adult zebrafish skeletal myosin step-size and step-frequency [11].
772 ELC N-terminus binding to actin is the mechanism for generating the 3 unitary steps [5] that is
773 modeled in a 4-pathway network in **Fig 8**.

774 In vivo step-size and step-frequency from auxotonic and near-isometric cardiac myosin in
775 **Fig 7 panels a & b** indicates step-sizes of ~2, 4 and 6 nm paralleling the unloaded in vitro

776 estimates of ~3, 5, and 8 for porcine cardiac myosin plus a force producing 0 length step unique
777 to the native in vivo environment. Strain in the active cardiac myosin under load probably lowers
778 measured in vivo step-sizes by affecting the apparent lever-arm rotation angle Φ and also
779 causing the 0 length step. The step-size and step-frequency data from **Fig 7 panels a & b** are
780 interpreted in **Fig 8** showing myosin flux through the 4-pathway network for unloaded,
781 auxotonic, and near-isometric phases of cardiac muscle contraction. Increasing load (smaller net
782 force or velocity **v**) changes step-frequencies to favor shorter steps such that in near-isometric
783 conditions the long 8 nm step is practically eliminated, the 5 nm step is down-regulated from the
784 unloaded value of 43 to 12%, while the shortest 3 nm step is up-regulated from the unloaded
785 value of 5 to 80% of the total steps (**Table 2**). Uniquely, the 5 then 3 nm step up regulates then
786 down regulates when the muscle transitions from unloaded to isometric phases suggesting its
787 role is to better accommodate rapidly changing force production conditions when the 8 nm step
788 is too long but the 3 nm step is too short to maintain power requirements. That the 3 nm exceeds
789 5 nm step-frequency under high load implied the new mechanism for step-size generation where
790 the 3 nm step contributes both independently and together with the 5 nm step. This is unlike
791 previous assertions that the 3 nm step strictly follows on the 5 nm step based on in vitro work
792 [5]. Increasing load also causes the muscle to make use of the force producing 0 length step that
793 holds tension by remaining strongly actin bound when sliding velocity is near zero. We find that
794 the correlation of rising 0 length and 3 nm step-frequencies with lower 5 and 8 nm step-
795 frequencies and higher resisting force implicates the ELC N-terminus and strained rigor
796 conformation in strain sensing. This observation could be at odds with earlier in vitro motility
797 work looking at strain-dependence in mouse cardiac myosin under load where strain enhanced
798 ATP affinity for actomyosin [44] although loads were short of near-isometric where the ELC
799 ratchet is expected to lower ATP affinity for actomyosin. The video file in S5Movie has an
800 audio/visual description/representation of myosin flux through the 4-pathway network during
801 unloaded, auxotonic, and near-isometric contraction. The written description for the S5 Movie is
802 in S2 File. The latter elaborates on the audio portion of the movie and contains one equation.

803 The proposed mechanisms for strain sensing in vivo, depicted in **Fig 8**, has the ELC
804 ratchet causing the time extended strained rigor state by inhibiting ATP binding, and, the strain
805 dependent ADP release causing the time extended ADP state by inhibiting ADP release. The
806 ELC mediated mechanism accounts for most (42 of 52%) of the total flux into the force

producing 0 length step in near-isometric phase. The inhibition efficiency of the strain dependent mechanisms, defined as the flux into the 0 length step divided by the total flux through the contributing pathway, suggests that the strain-dependent ADP release mechanism shuts down flux to the 0 length step pathway from the 5 nm step pathway. Instead the flux travels through the less inhibiting ELC ratchet mediated strain dependent mechanism.

Conclusion

Cardiac ventriculum myosin transitioning from low to high force causes motor down-shifting to a 3 nm step-size accounting for >80% of all steps in the near-isometric contraction phase. We propose that strain delays ATP dissociation of actomyosin at isometric force using a mechanism involving the ratcheting effect of the actin bound ELC N-terminus. The significance of ELC N-terminus actin binding follows directly from earlier in vitro single myosin measurements [5, 17] showing close correlation between in vitro and in vivo systems. Enhanced occupation of the 0 length step hints at a mechanism for restrictive cardiomyopathy (RCM) caused by mutation in ELC [45]. Strongly bound myosins fail to detach quickly due to a fault in the ELC N-terminus strain sensing inhibiting detachment under low load conditions. It produces a drag force during stretch when the muscle should be fully relaxed.

We explored transduction/mechanical coupling in the beating heart at the single myosin level. High time resolution imaging captures and discriminates the native single myosin behavior during auxotonic and isometric phases of its contractile cycle providing deep insight into the significance of the cardiac myosin strain dependent biochemistry. Overall our approach provides a unique bottom-up assessment of the muscle motor performance by combining high precision single myosin mechanical characterization in an integrated and hierarchically functioning native muscle machine.

832 DISCLOSURE

833 We have no competing interests.

834

835 Supporting information

836 S1 File. S1 File consists of two figures (A &B) with captions.

837 S2 File. S2 File contains a description of S5 Movie.

838 S1 Movie. S1 Movies contains the video Data147bs(43,171,38,106,90)1.avi.

839 S2 Movie. S2 Movie contains the video Data149bs(190,180,67,121,90)1.avi.

840 S3 Movie. S3 Movie contains the video Data1bs(182,168,98,163,55)1.avi.

841 S4 Movie. S4 Movie contains the video Data230bs(214,217,61,110,45)3.avi.

842 S5 Movie. S5 Movies contains the video Movie5.wmv.

843

844

References

1. Huxley HE. The mechanism of muscular contraction. Science. 1969;164:1356-66.

2. Pant K, Watt J, Greenberg M, Jones M, Szczesna-Cordary D, Moore JR. Removal of the cardiac myosin regulatory light chain increases isometric force production. The FASEB Journal. 2009;23:3571-80.

3. Burghardt TP, Sikkink LA. Regulatory light chain mutants linked to heart disease modify the cardiac myosin lever-arm. Biochemistry. 2013;52:1249-59.

4. Lossie J, Köhncke C, Mahmoodzadeh S, Steffen W, Canepari M, Maffei M, et al. Molecular mechanism regulating myosin and cardiac functions by ELC. Biochem Biophys Res Commun. 2014;450(1):464-9.

5. Wang Y, Ajtai K, Kazmierczak K, Szczesna-Cordary D, Burghardt TP. N-terminus of Cardiac Myosin Essential Light Chain Modulates Myosin Step-Size. Biochemistry. 2015;55:186-98.

6. Burghardt TP, Ajtai K, Chan DK, Halstead MF, Li J, Zheng Y. GFP tagged regulatory light chain monitors single myosin lever-arm orientation in a muscle fiber. Biophys J. 2007;93:2226-39.

7. Burghardt TP, Josephson MP, Ajtai K. Single myosin cross-bridge orientation in cardiac papillary muscle detects lever-arm shear strain in transduction. Biochemistry. 2011;50:7809-21.

8. Tokunaga M, Imamoto N, Sakata-Sogawa K. Highly inclined thin illumination enables clear single-molecule imaging in cells. Nature Methods. 2008;5:159-61.

9. Huang C-J, Tu C-T, Hsiao C-D, Hsieh F-J, Tsai H-J. Germ-line transmission of a myocardium-specific GFP transgene reveals critical regulatory elements in the cardiac myosin light chain 2 promoter of zebrafish. Dev Dyn. 2003;228(1):30-40.

10. Sun X, Ekker SC, Shelden EA, Takubo N, Wang Y, Burghardt TP. In vivo orientation of single myosin lever-arms in zebrafish skeletal muscle. Biophys J. 2014;107:1403-14.

11. Burghardt TP, Ajtai K, Sun X, Takubo N, Wang Y. In Vivo Myosin Step-Size from Zebrafish Skeletal Muscle. Open Biology. 2016;6:160075.

12. Chen Z, Huang W, Dahme T, Rottbauer W, Ackerman MJ, Xu X. Depletion of zebrafish essential and regulatory myosin light chains reduces cardiac function through distinct mechanisms. Cardiovasc Res. 2008;79(1):97-108.

13. Zhang J, Wilson GF, Soerens AG, Koonce CH, Yu J, Palecek SP, et al. Functional Cardiomyocytes Derived From Human Induced Pluripotent Stem Cells. Circ Res. 2009;104(4):e30-e41.

14. Boulter N, Suarez FG, Schibeci S, Sunderland T, Tolhurst O, Hunter T, et al. A simple, accurate and universal method for quantification of PCR. BMC Biotechnology. 2016;16(1):1-14.

884 **15. Marti-Renom MA, Stuart AC, Fiser A, Sanchez R, Melo F, Sali A. Comparative**
885 **protein structure modeling of genes and genomes. AnnuRevBiophysBiomolStruct.**
886 **2000;29:291-325.**

887 **16. Rayment I, Rypniewski WR, Schmidt-Base K, Smith R, Tomchick DR, Benning**
888 **MM, et al. Three-dimensional structure of myosin subfragment-1: A molecular motor.**
889 **Science. 1993;261:50-8.**

890 **17. Wang Y, Ajtai K, Burghardt TP. Qdot labeled actin super-resolution motility assay**
891 **measures low duty cycle muscle myosin step-size. Biochemistry. 2013;52:1611-21.**

892 **18. Steffen W, Smith D, Simmons R, Sleep J. Mapping the actin filament with myosin.**
893 **Proc Natl Acad Sci USA. 2001;98:14949-54.**

894 **19. Timson DJ, Trayer HR, Trayer IP. The N-terminus of A1-type myosin essential**
895 **light chains binds actin and modulates myosin motor function. Eur J Biochem.**
896 **1998;255:654-62.**

897 **20. Muthu P, Wang L, Yuan C-C, Kazmierczak K, Huang W, Hernandez OM, et al.**
898 **Structural and functional aspects of the myosin essential light chain in cardiac muscle**
899 **contraction. FASEB J. 2011;25(12):4394-405.**

900 **21. Petzhold D, Simsek B, Meißner R, Mahmoodzadeh S, Morano I. Distinct**
901 **interactions between actin and essential myosin light chain isoforms. Biochem Biophys Res**
902 **Commun. 2014;449(3):284-8.**

22. Siemankowski RF, White HD. Kinetics of the interaction between actin, ADP, and cardiac myosin-S1. J Biol Chem. 1984;259(8):5045-53.

23. Moczarska A, Kakol I. The influence of regulatory light chains on structural organization of cardiac myosin heads interacting with actin and ATP. BiochemMolBiolInt. 1995;37(4):765-72.

24. Kazmierczak K, Xu YY, Jones M, Guzman G, Hernandez OM, Kerrick WGL, et al. The role of the N-terminus of the myosin essential light chain in cardiac muscle contraction. J Mol Biol. 2009;387(3):706-25.

25. Wendt T, Taylor D, Trybus KM, Taylor K. Three-dimensional image reconstruction of dephosphorylated smooth muscle heavy meromyosin reveals asymmetry in the interaction between myosin heads and placement of subfragment 2. Proc Natl Acad Sci USA. 2001;98(9):4361-6.

26. Al-Khayat HA, Kensler RW, Squire JM, Marston SB, Morris EP. Atomic model of the human cardiac muscle myosin filament. Proc Natl Acad Sci USA. 2013;110(1):318-23.

27. Alamo L, Qi D, Wriggers W, Pinto A, Zhu J, Bilbao A, et al. Conserved intramolecular interactions maintain myosin interacting-heads motifs explaining tarantula muscle super-relaxed state structural basis. J Mol Biol. 2016;428(6):1142-64.

28. Bobroff N. Position measurement with a resolution and noise-limited instrument. Rev Sci Instrum. 1986;57:1152-7.

29. Burghardt TP. Single molecule fluorescence image patterns linked to dipole orientation and axial position: Application to myosin cross-bridges in muscle fibers. Plos One. 2011;6:e16772.

30. Burghardt TP, Thompson NL. Motion of myosin cross-bridges in skeletal muscle fibers studied by time-resolved fluorescence anisotropy decay. Biochemistry. 1985;24:3731-5.

31. Burghardt TP, Sun X, Wang Y, Ajtai K. In vitro and in vivo single myosin step-sizes in striated muscle. J Muscle Res Cell Motil. 2016:1-15.

32. Wang Y, Ajtai K, Burghardt TP. Ventricular myosin modifies in vitro step-size when phosphorylated. J Mol Cell Cardiol. 2014;72:231-7.

33. Piazzesi G, Lucii L, Lombardi V. The size and the speed of the working stroke of muscle myosin and its dependence on the force. J Physiol (Lond). 2002;545(1):145-51.

34. Borejdo J, Putnam S, Morales MF. Fluctuations in polarized fluorescence: Evidence that muscle cross bridges rotate repetitively during contraction. Proceedings of the National Academy of Sciences. 1979;76:6346-50.

35. Irving M, Allen TSC, Sabido-David C, Cralk JS, Brandmeler B, Kendrick-Jones J, et al. Tilting of the light-chain region of myosin during step length changes and active force generation in skeletal muscle. Nature. 1995;375:688-90.

36. Burghardt TP, Garamszegi SP, Ajtai K. Probes bound to myosin Cys-707 rotate during length transients in contraction. Proceedings of the National Academy of Sciences. 1997;94:9631-6.

37. Reconditi M, Linari M, Lucii L, Stewart A, Sun Y, Boesecke P, et al. The myosin motor in muscle generates a smaller and slower working state at higher load. Nature. 2004;428:578-81.

38. Finer JT, Simmons RM, Spudich JA. Single myosin molecule mechanics: piconewton forces and nanometre steps. Nature. 1994;368:113-9.

39. Kaya M, Higuchi H. Nonlinear elasticity and an 8-nm working stroke of single myosin molecules in myofilaments. Science. 2010;329(5992):686-9.

40. González-Solá M, Al-Khayat Hind A, Behra M, Kensler Robert W. Zebrafish cardiac muscle thick filaments: isolation technique and three-dimensional structure. Biophys J. 2014;106(8):1671-80.

41. Jung HS, Komatsu S, Ikebe M, Craig R. Head-head and head-tail interaction: A general mechanism for switching off myosin II activity in cells. Mol Biol Cell. 2008;19(8):3234-42.

42. Hooijman P, Stewart MA, Cooke R. A new state of cardiac myosin with very slow ATP turnover: A potential cardioprotective mechanism in the heart. Biophys J. 2011;100(8):1969-76.

43. Craig R, Padron R, Kendrick-Jones J. Structural changes accompanying phosphorylation of tarantula muscle myosin filaments. The Journal of Cell Biology. 1987;105(3):1319-27.

44. Greenberg MJ, Kazimierczak K, Szczesna-Cordary D, Moore JR. Cardiomyopathy-linked myosin regulatory light chain mutations disrupt myosin strain-dependent biochemistry. Proc Natl Acad Sci USA. 2010;107(40):17403-8.

45. Olson TM, Karst ML, Whitby FG, Driscoll DJ. Myosin light chain mutation causes autosomal recessive cardiomyopathy with mid-cavitary hypertrophy and restrictive physiology. Circulation. 2002;105(20):2337-40.

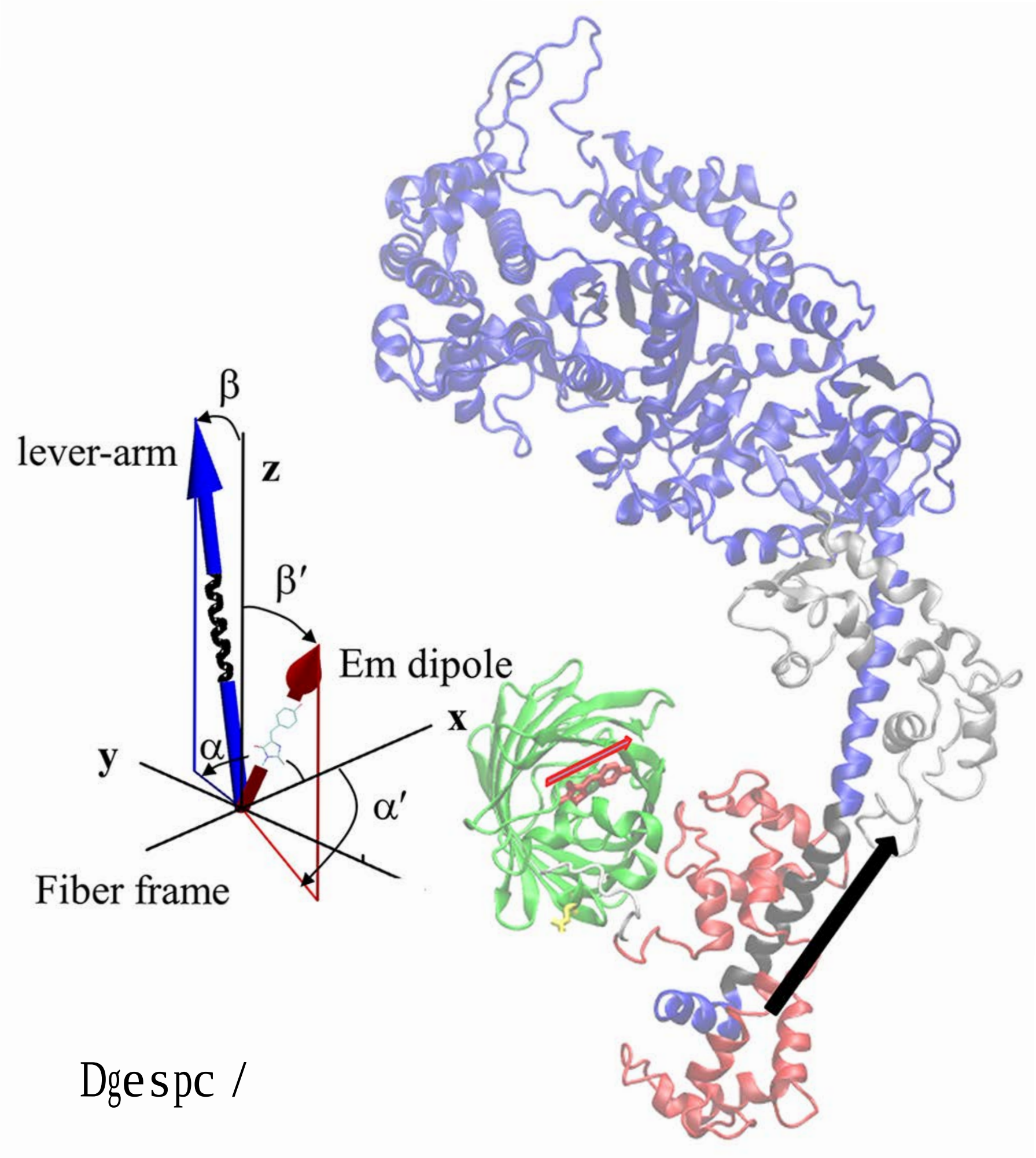

Dgespc /

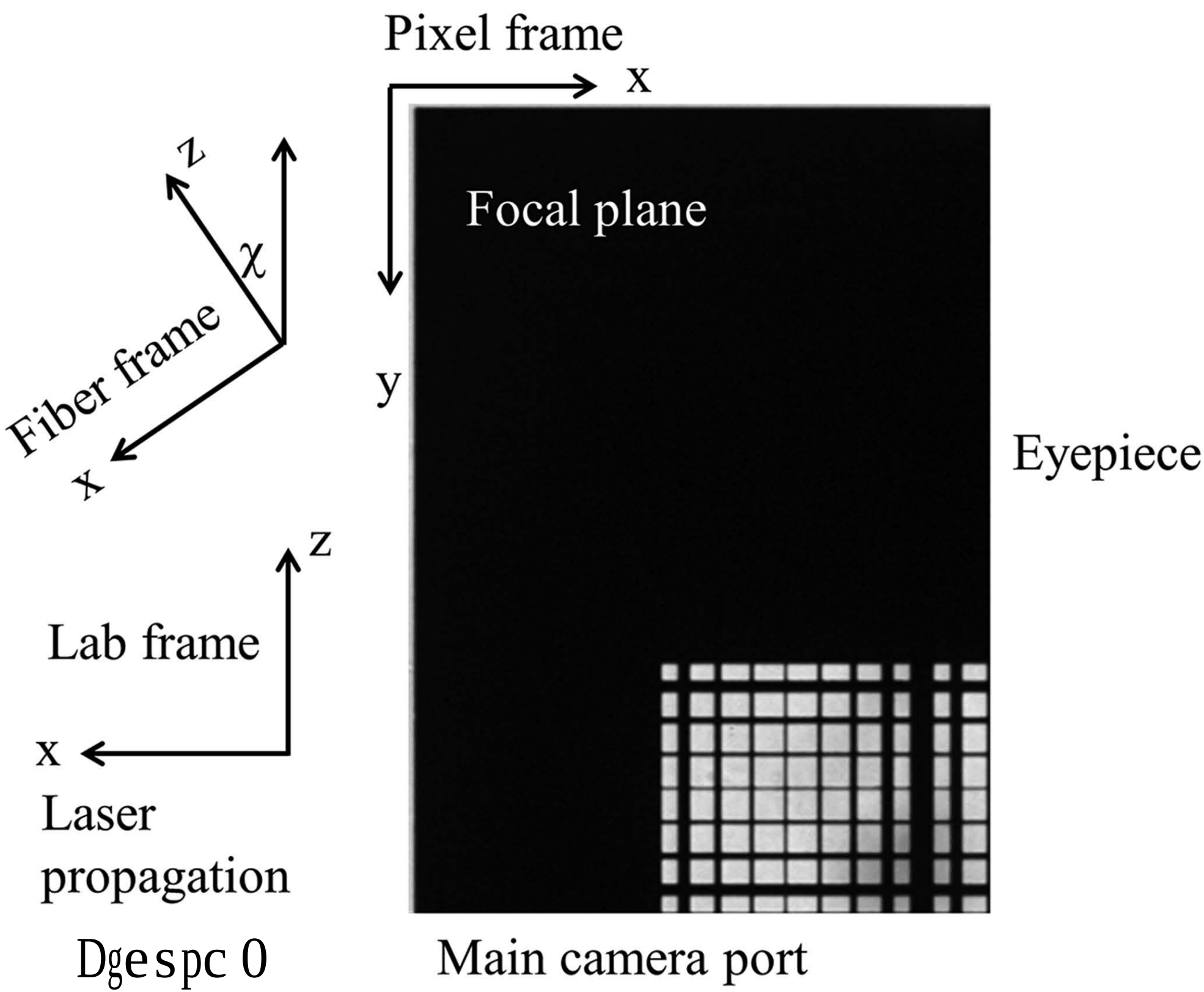
Pixel frame
x
y
Focal plane
Eyepiece
z
χ
Fiber frame
x
z
Lab frame
x
Laser
propagation
Dgespc 0
Main camera port

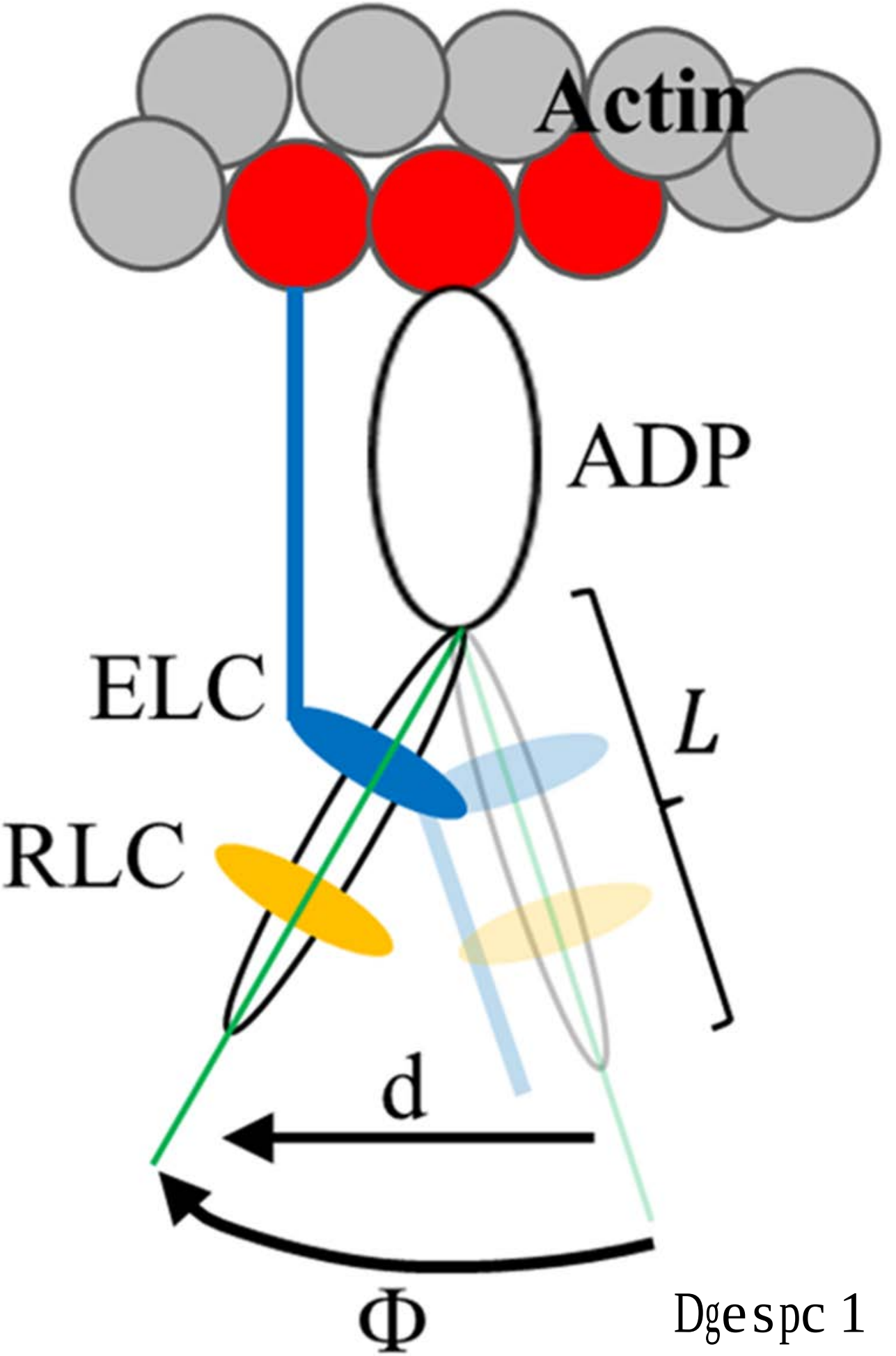

Dgespc 1

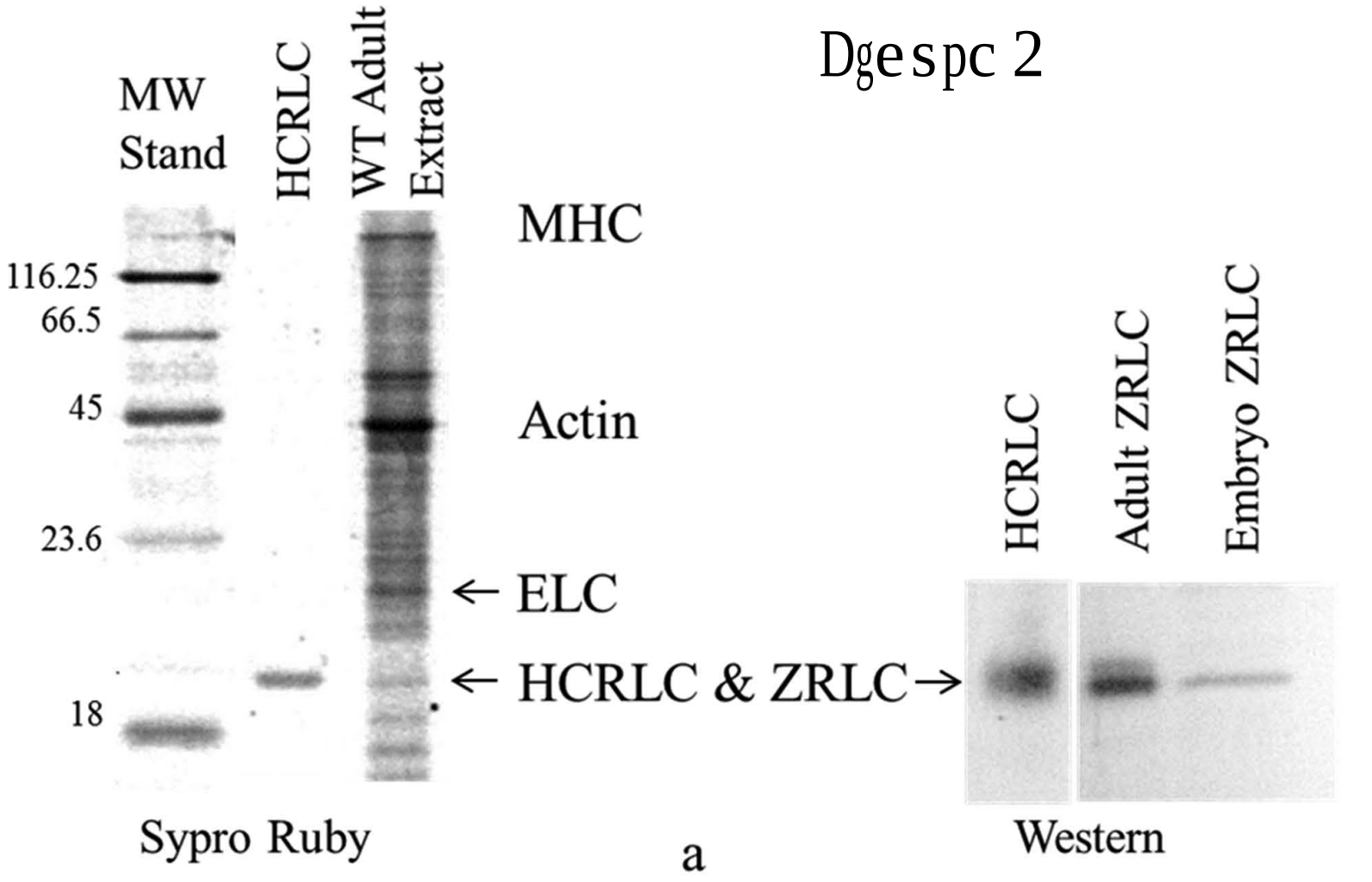
MW Stand
HCRLC
WT Adult Extract
MHC
116.25
66.5
45
Actin
23.6
← ELC
← HCRLC & ZRLC →
18
Sypro Ruby
a
HCRLC
Adult ZRLC
Embryo ZRLC
Western

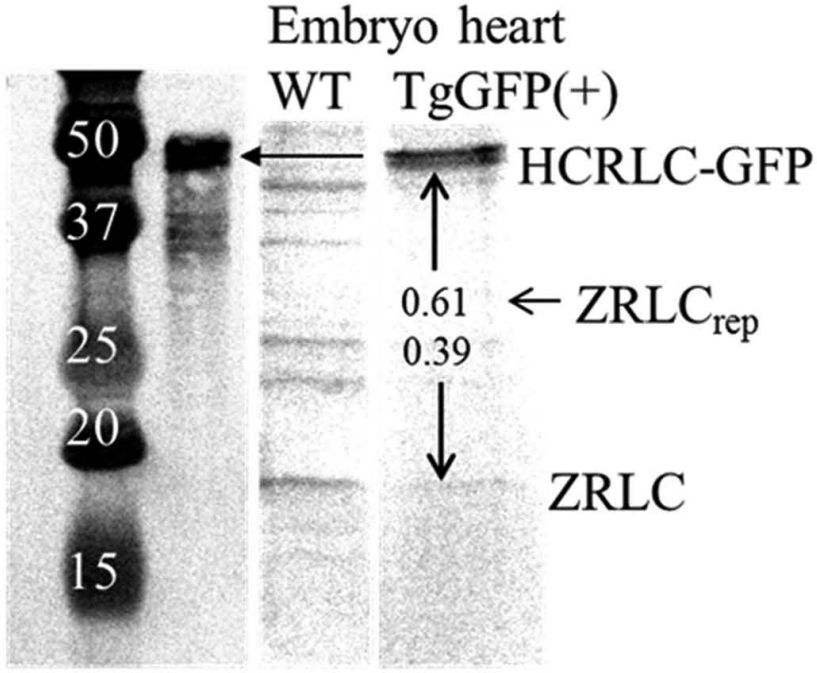
Embryo heart
WT
TgGFP(+)
50
37
25
20
15
HCRLC-GFP
0.61
← ZRLC$_{rep}$
0.39
ZRLC
b

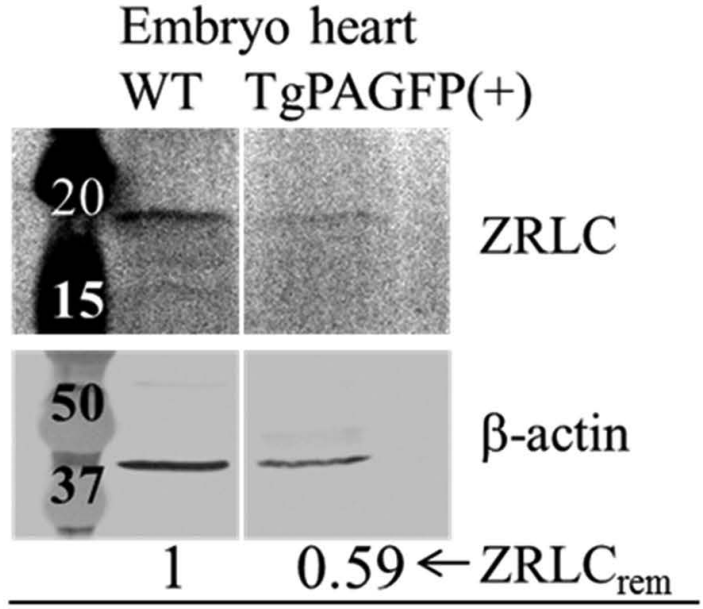
Embryo heart
WT
TgPAGFP(+)
20
15
ZRLC
50
37
β-actin
1
0.59 ← ZRLC$_{rem}$
c

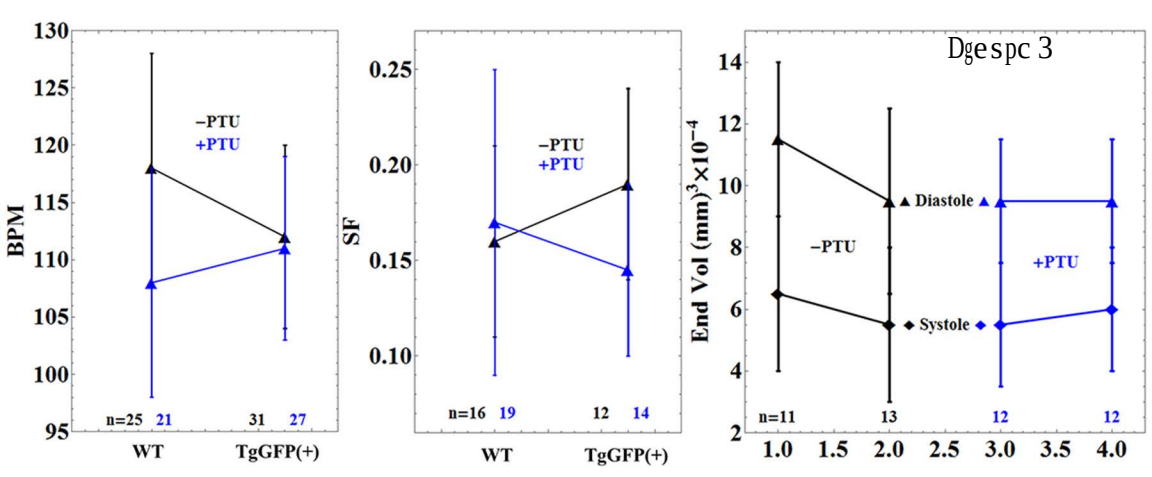
Dgespc 3
BPM
SF
End Vol (mm)^3×10^{-4}
−PTU
+PTU
Diastole
Systole
n=25 21 31 27
n=16 19 12 14
n=11 13 12 12
WT
TgGFP(+)

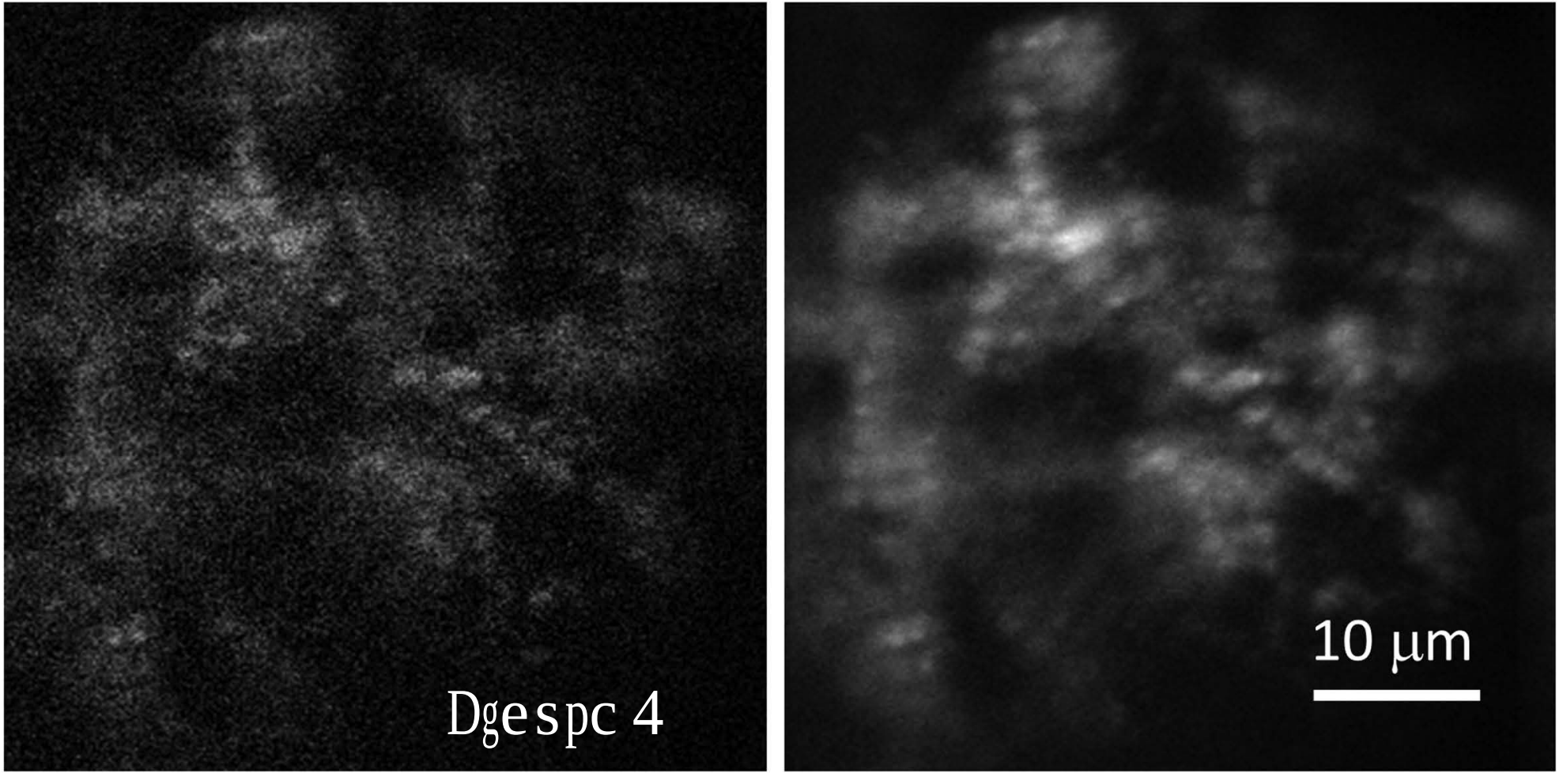
Dgespc 4
10 μm

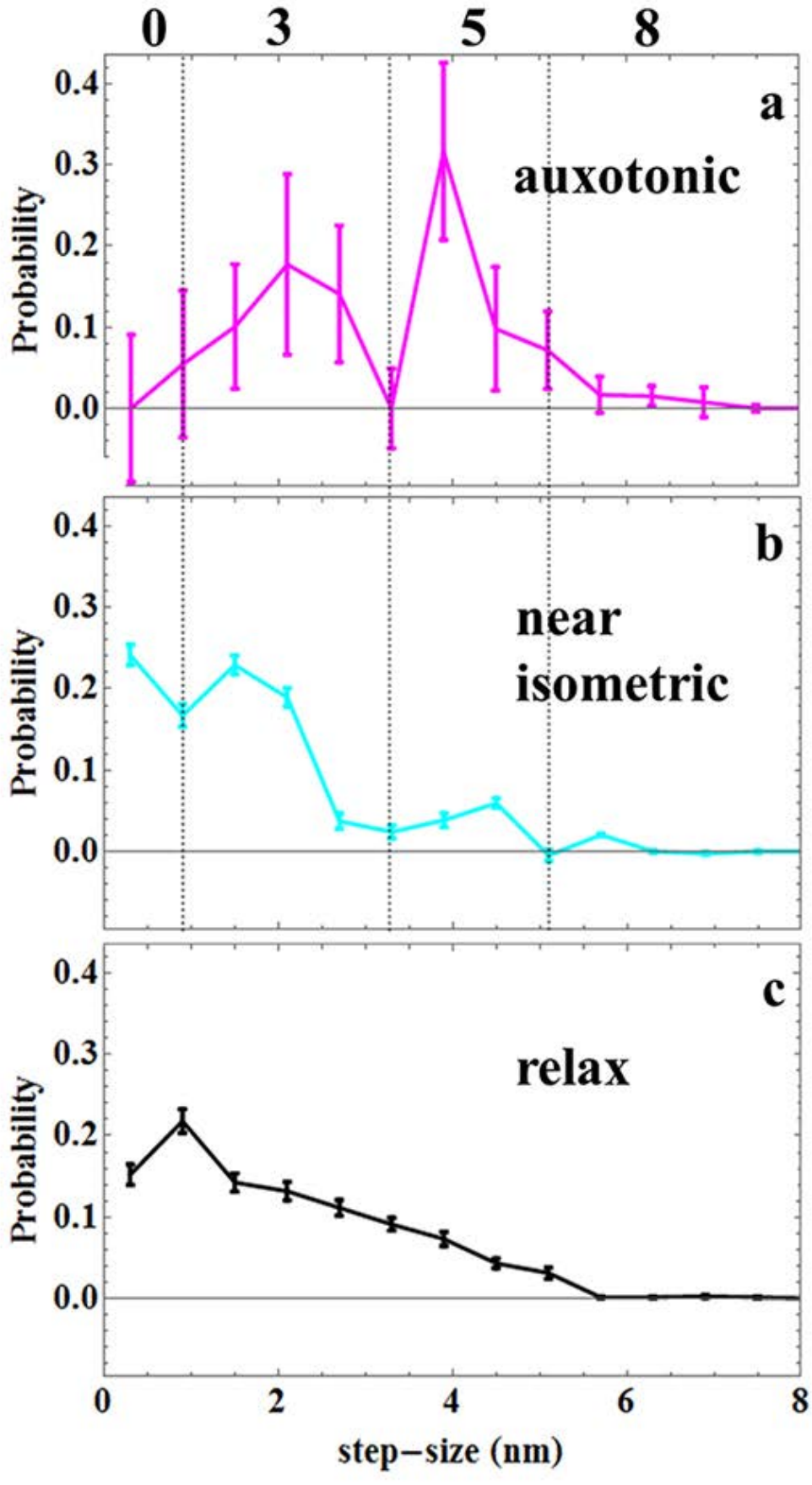
0
3
5
8
a
auxotonic
b
near
isometric
c
relax
Probability
0.4
0.3
0.2
0.1
0.0
0
2
4
6
8
step−size (nm)

Dgespc 5

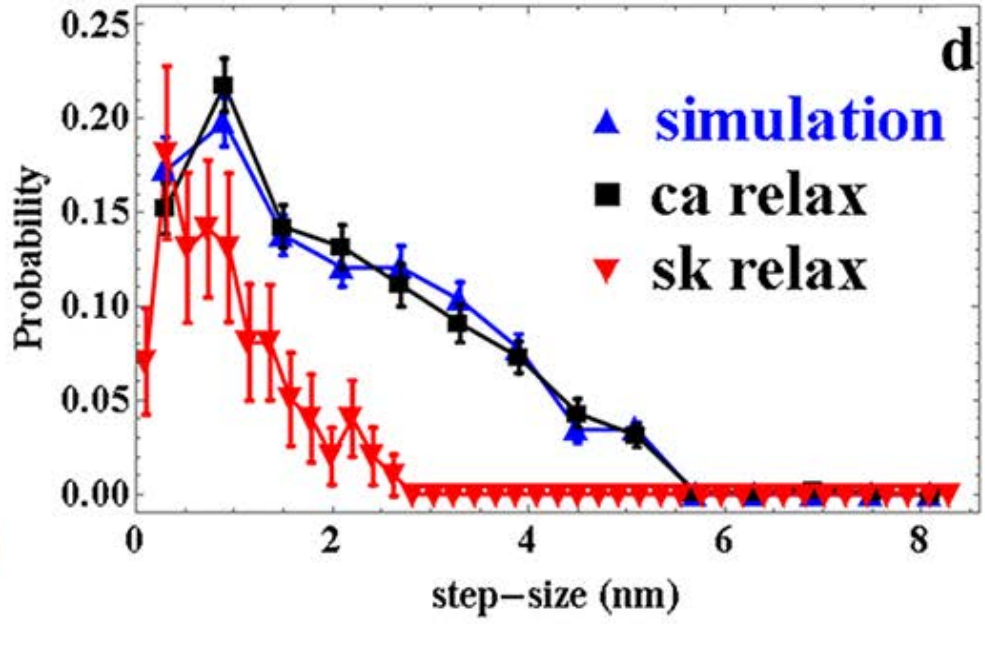
d
simulation
ca relax
sk relax
Probability
0.25
0.20
0.15
0.10
0.05
0.00
0
2
4
6
8
step−size (nm)

Figure 8

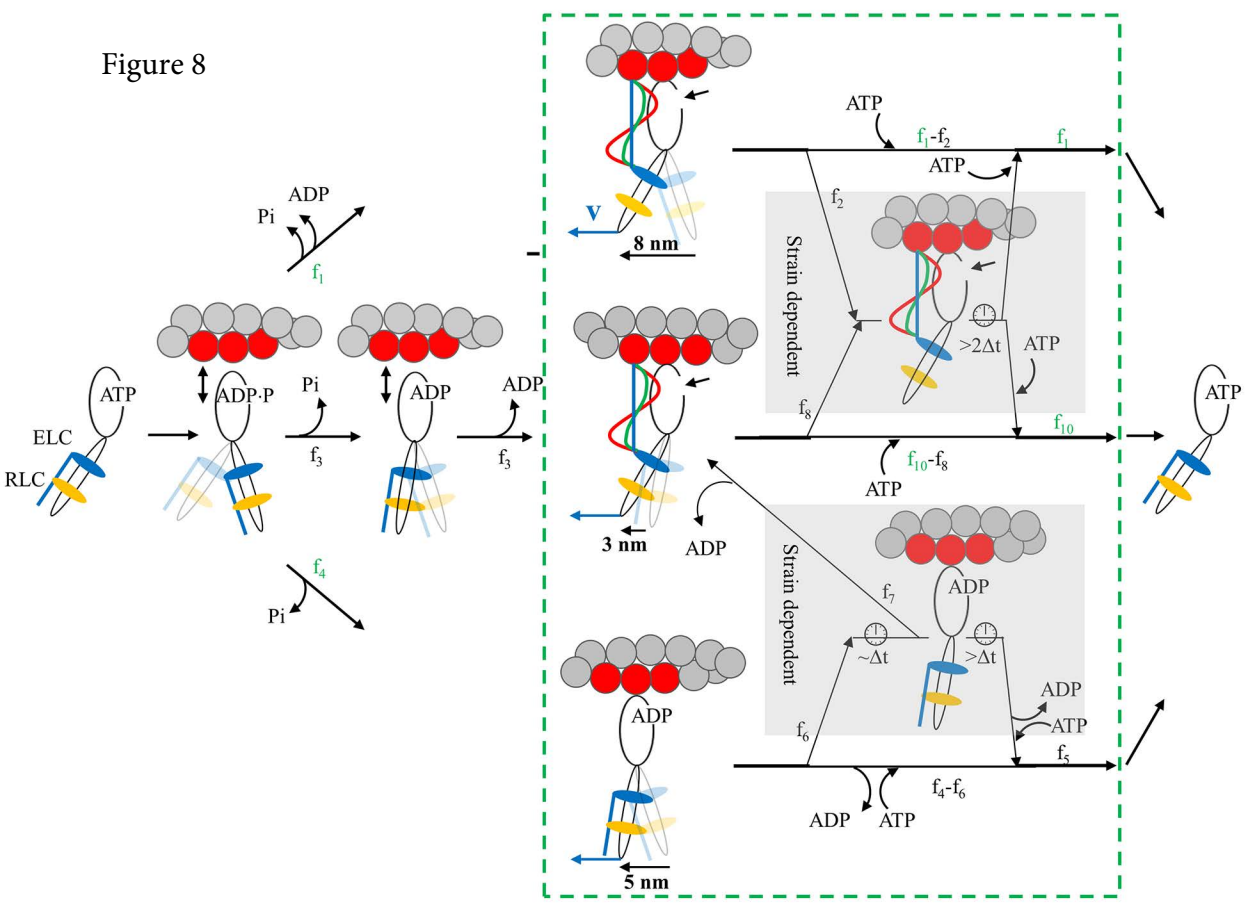
ADP
Pi
f_1
ATP
ELC
RLC
ADP·P
Pi
f_3
ADP
ADP
f_3
f_4
Pi
V
8 nm
3 nm
5 nm
ADP
ATP
f_1-f_2
f_1
ATP
f_2
Strain dependent
>2Δt
ATP
f_8
f_{10}
f_{10}-f_8
ATP
ATP
ADP
Strain dependent
f_7
ADP
~Δt
>Δt
ADP
ATP
f_6
f_5
f_4-f_6
ADP
ATP